

Article

Stabilization of Pt in SiO₂–Al₂O₃ Microspheres at High Mechanical Resistance, Promoted with W Oxides for the Combustion of CO

Arturo Pallares-García ¹, José Luis Contreras ^{1,*}, Jennipher Pérez-Cabrera ¹, Beatriz Zeifert ², Tamara Vázquez ², José Salmones ² and Miguel Angel Gutiérrez-Limón ¹ 

¹ Department of Energy, CBI, Metropolitan Autonomous University-Azcapotzalco, Av. San Pablo 180, Col. Reynosa, México City C.P. 02200, Mexico; rotuar20@hotmail.com (A.P.-G.); jennipc010@gmail.com (J.P.-C.); magl@azc.uam.mx (M.A.G.-L.)

² Department of Engineering in Metallurgy and Materials, ESIQIE, National Polytechnic Institute, Av. IPN Col. Lindavista, Mexico City C.P. 07738, Mexico; bzeifert@yahoo.com (B.Z.); avazquezrdz@hotmail.com (T.V.); jose_salmones@yahoo.com.mx (J.S.)

* Correspondence: jlcl@azc.uam.mx; Tel.: +52-1-5591911047

Abstract: This study shows the development of a combustion promoter for the oil-refining process called fluid catalytic cracking (FCC). The investigation of a catalyst prepared for the combustion of CO composed of 0.05 wt% Pt supported on SiO₂–Al₂O₃–0.5 wt% W microspheres with high mechanical resistance, promoted with tungsten oxides (WO_x) that can inhibit the sintering of Pt, is reported. The addition of WO_x in SiO₂–Al₂O₃ inhibited the decrease in the specific area when calcined from 550 °C to 950 °C. SiO₂–Al₂O₃ support in the form of calcined microspheres with average diameters between 70–105 μm were produced by spray drying, using two atomization discs with vanes of different geometry: a straight rectangular blade disc (DAR) and a curved rectangular vanes disc (DAC). The DAR disk produced whole microspheres, while the DAC had hollow and broken microspheres. The microspheres were characterized by XRD, SEM, optical microscopy, N₂ physisorption (BET area) and fracture resistance tests. The Pt catalysts were evaluated by TPR, H₂ chemisorption and CO combustion. The catalyst of 0.05 wt% Pt/SiO₂–Al₂O₃–0.5 wt% turned out to be the most stable. A thermal stabilization effect was observed at contents lower than 1 wt% W that allowed it to inhibit the sintering of the Pt catalyst.

Keywords: CO combustion promoter; Pt/SiO₂–Al₂O₃–WO_x catalyst; spherical particles; spray drying; rotary atomizer disks



Citation: Pallares-García, A.; Contreras, J.L.; Pérez-Cabrera, J.; Zeifert, B.; Vázquez, T.; Salmones, J.; Gutiérrez-Limón, M.A. Stabilization of Pt in SiO₂–Al₂O₃ Microspheres at High Mechanical Resistance, Promoted with W Oxides for the Combustion of CO. *Catalysts* **2021**, *11*, 1320. <https://doi.org/10.3390/catal11111320>

Academic Editor: Vincenzo Vaiano

Received: 16 August 2021

Accepted: 28 October 2021

Published: 30 October 2021

Publisher's Note: MDPI stays neutral with regard to jurisdictional claims in published maps and institutional affiliations.



Copyright: © 2021 by the authors. Licensee MDPI, Basel, Switzerland. This article is an open access article distributed under the terms and conditions of the Creative Commons Attribution (CC BY) license (<https://creativecommons.org/licenses/by/4.0/>).

1. Introduction

Most fluid catalytic cracking (FCC) units in the oil industry have introduced additives that improve the performance of the cracking catalyst. The main benefits of adding additives in FCC units are to improve unit performance and reduce the amount of polluting gases emitted by the regenerator into the atmosphere [1–5]. In particular, the CO combustion promoter additive is added to the inventory of the cracking catalyst or within the regenerator of the FCC unit to catalyze the oxidation reaction of CO to CO₂ into the dense phase of the regenerator, reducing the high residual concentration of CO in the flue gas released by the regenerator [6–11]. This additive contributes to the regeneration of the cracking catalyst contaminated with coke through a more efficient and uniform burning, facilitating fluidization of the cracking catalyst and controlling post-combustion problems that take place in the diluted phase of the regenerator [12–14].

Commercial CO combustion promoters are made up of attrition-resistant fluidizable spherical particles, such as alumina (Al₂O₃), silica–alumina (SiO₂/Al₂O₃), or mixed oxides, which are produced by the spray-drying process with specific physical properties, such as a particle size range between 20 to 180 μm and a particle mean size between 75 to 80 μm,

in which the powder conformed by these particles must have a high density [5,10,11,13,15]. Such physical properties are achieved through an adequate control of the atomization parameters of the suspension with a chosen material, the operation parameters of the spray drying, and subsequent sieving of the product to recover the portion of the particles with the desired sizes.

In addition, the calcination temperatures of the microspheres range from 700 to 1150 °C, depending on the material they are made of. Calcination causes the microspheres to achieve greater hardness and the powders to acquire the desired textural properties, such as specific areas between 85 to 95 m²/g, pore volumes between 0.30 to 0.38 cm³/g, and average pore diameters between 15 to 35 nm, with the purpose that said particles are compatible with the reaction and regeneration steps of the FCC units [10,11,15]. Subsequently, the impregnation of the Pt-active metal is carried out on the surface of the calcined microspheres in concentrations ranging from 300 to 1500 ppm [1,6,7,11,12,14,16] as well as other noble metals that have been used such as Ir, Os, Pd, Ru, Rh, and Au [3,6].

It is known that spray drying is the most commonly used technology for the manufacture of microspheres [17] in various industries associated with the processing of ceramic [18], food, chemical, mineral, and pharmaceutical products, among others [19]. Spray drying consists of transforming a feed in a fluid state into a spray of drops, which come into contact with a stream of hot gas (generally air) to generate a powder with a specific particulate form. In this process, the atomizer is responsible for continuously producing the dispersion of millions of drops. The atomizers commonly used in spray drying are spray nozzles, rotary atomizers, sonic nozzles, and electrohydrodynamic atomizers [20–22]. The choice of atomizer will depend on the design of the dryer, the processing capabilities, and the required product specifications.

In particular, the rotary atomizer is used in many industries to atomize fluids of various nature. The rotating atomizer disk is responsible for spraying drops. Atomization of fluid with a disc occurs when the disk rotates at high rotational speeds, such as 3000 to 50,000 rpm [23], where the liquid is injected into the disk's center. Subsequently, the liquid slides at high speed over the disk's walls, as a thin film, due to centrifugal force, and it is confined through the ejection channels of the disk, to finally disintegrate the film into a spray at the edge of the disk [20–22,24–28]. Currently, there are numerous designs of atomizer disks that fulfill the requirements of capacity and quality of the final product; however, we will focus on just two: the straight rectangular vanes disk and the curved rectangular vanes disk.

On the other hand, due to the high thermal stability requirements for the development of this CO combustion promoter catalyst of Pt/SiO₂–Al₂O₃–WO_x, we have made previous studies with the addition of structural promoters such as tungsten oxides (WO_x) [29–31], where it has been found that at low concentrations of W (<1 wt%), it is possible to stabilize Al₂O₃ and Pt particles.

The present study contributes to improving the Pt/Al₂O₃ catalyst by adding minimal amounts of Pt and WO_x on SiO₂–Al₂O₃, which enhances the combustion of CO. The Pt/SiO₂–Al₂O₃–WO_x catalysts were prepared in the form of microspheres obtained by spray drying a SiO₂–Al₂O₃ suspension, using a straight rectangular vanes atomizer disk and a curved rectangular vanes atomizer disk. In the experiments, the rotation speed of the atomizer disks was varied, ranging from 3000 to 14,000 rpm. The effects of the rotation speed and the vanes geometry of the atomization disks on the morphology of the microspheres and some physical and textural properties of the synthesized SiO₂–Al₂O₃–WO_x powders were studied.

The microspheres with the optimal amount of WO_x obtained a high metallic dispersion of Pt (500 ppm), and they were also resistant to high-temperature calcination, stabilizing the porous structure. The combination of the precursors in the gel of the oxides of SiO₂–Al₂O₃ turned out to be the best procedure for high compression crushing strength. The best prototype turned out to be a macrosphere with a ratio of 25 wt% SiO₂ and 75 wt% Al₂O₃. This prototype was used to prepare the feed suspension for spray

drying. Therefore, it was possible to determine which design and disk rotation speed were the most convenient for the catalyst to promote CO combustion. Finally, it was observed that although WO_x stabilizes the Pt particles at high temperatures, at high concentrations of WO_x , the dispersion of Pt decreases. Therefore, the concentration of W was an essential factor to the preparation of the best CO combustion promoter.

2. Results and Discussion

This study begins with the results of the mechanical resistance of the $SiO_2-Al_2O_3$ microspheres prepared with different concentrations of SiO_2 and Al_2O_3 and the results of the characterization of the oxides of $SiO_2-Al_2O_3$ by DRX and N_2 physisorption.

Results of the preparation of Al_2O_3 and $SiO_2-Al_2O_3$ microspheres of a fixed concentration by spray-drying technology are also presented, studying two-vane disks with different geometry. These disks were operated at different rotation speeds to find the most suitable atomization parameters for obtaining microspheres with diameters ranging from 20–180 μm , trying to reach an average diameter between 75 and 80 μm . The characterization of Pt catalysts promoted with W oxides (WO_x) supported on $SiO_2-Al_2O_3$ microspheres was made by DRX, temperature-programmed reduction (TPR), and H_2 chemisorption to evaluate the dispersion of active Pt presented. Finally, the results of the catalytic combustion of CO are presented.

2.1. Crushing Strength of the $SiO_2-Al_2O_3$ Macrospheres

It was observed from the mixtures of gels of silicic acid and boehmite that when increasing the concentration of SiO_2 , the crushing strength by compression of the macrospheres of $SiO_2-Al_2O_3$ (3 mm of diameter) increased gradually (Figure 1). The macrosphere that was prepared from the mixture 25SA presented a crushing strength of 138.4 N, above the crushing strength of the macrosphere that was determined with commercial Al_2O_3 , which was 116 N.

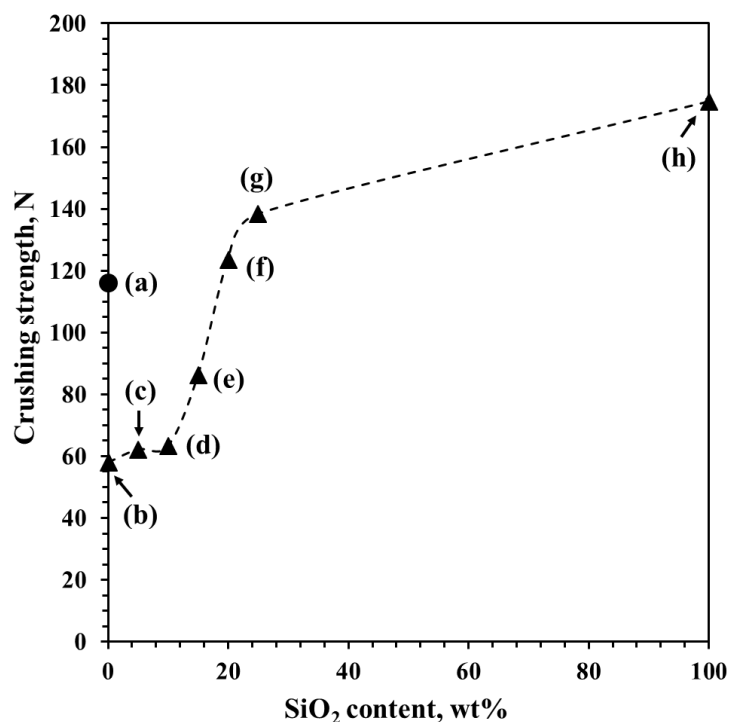


Figure 1. Tests of crushing strength of the macrospheres calcinated at 550 °C: (a) commercial Al_2O_3 , (b) Al_2O_3 (100A), (c) 5 wt% SiO_2-95 wt% Al_2O_3 (5SA), (d) 10 wt% SiO_2-90 wt% Al_2O_3 (10SA), (e) 15 wt% SiO_2-85 wt% Al_2O_3 (15SA), (f) 20 wt% SiO_2-80 wt% Al_2O_3 (20SA), (g) 25 wt% SiO_2-75 wt% Al_2O_3 (25SA) y (h) SiO_2 (100S). Resistance to rupture refers to spheres with a diameter of 3 mm. The relative error of the crushing strength was $\pm 0.5\%$.

2.2. Jet-Cup Attrition Tests of the $\text{SiO}_2\text{-Al}_2\text{O}_3$ Microspheres

For this test, $\text{SiO}_2\text{-Al}_2\text{O}_3$ microspheres were prepared by spray drying, which were calcined at 550 °C. The effect of the concentration of SiO_2 in Al_2O_3 with respect to the formation of fine particles of less than 20 μm (Table 1) was investigated, as an attrition test in a jet-cup type equipment [32]. The 25/75 selected support ($\text{SiO}_2/\text{Al}_2\text{O}_3$) showed less loss of fine particles (7.1%) than the other supports with lower SiO_2 concentrations. The support with a 20/80 ratio ($\text{SiO}_2/\text{Al}_2\text{O}_3$) presented a higher production of fines (8.2%).

Table 1. Fines percentage (<20 μm) obtained after jet-cup attrition test (for 1 h) of the $\text{SiO}_2\text{-Al}_2\text{O}_3$ microspheres.

Sample	wt% SiO_2	wt% Al_2O_3	After Jet-Cup Test (%)
100A	0	100	11.1
15SA	15.94	84.06	8.7
20SA	19.74	80.26	8.2
25SA	25.82	74.18	7.1

Although fine spheres may have a higher specific area and probably a higher catalytic activity, from our study of attrition losses of the microspheres, it was evidenced that in the selection of our support of 25/75 ($\text{SiO}_2/\text{Al}_2\text{O}_3$), the greatest resistance to attrition is achieved. This property is fundamental for this type of catalyst since it will be in motion in a fluidized bed. The resistance to attrition of the microspheres in jet-cup tests increases with the SiO_2 content. For these two reasons, we chose to use the solids of the mixture 25SA (25 wt% $\text{SiO}_2\text{-}75$ wt% Al_2O_3) for the preparation of this catalyst.

In the literature on combustion promoters [10,11,14,15], it has been mentioned as important property, having a support with the minor loss of fines derived from the collisions of the microspheres inside the regenerator of the FCC plant. The above means the loss of noble metal Pt, which implies a high cost and possible plugging problems in the filters in the output stream of the regenerator emissions.

2.3. Characterization of Oxides $\text{SiO}_2\text{-Al}_2\text{O}_3$

The X-ray diffraction patterns of $\text{SiO}_2\text{-Al}_2\text{O}_3$ oxides calcined at 550 °C exhibited reflections at 37°, 45°, 67° (Figure 2), which are typical of the $\gamma\text{-Al}_2\text{O}_3$ phase [33–35]. On the other hand, the characteristic reflection due to SiO_2 corresponds to a 2 θ value of 23° [36,37] identified with the JCPDS card 29-0085.

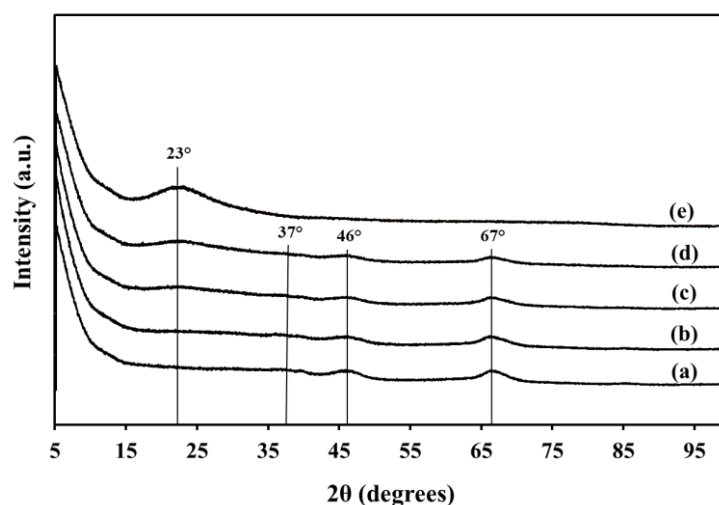


Figure 2. X-ray diffraction patterns of oxides calcined at 550 °C: (a) 100A, (b) 5SA, (c) 15SA, (d) 25SA y (e) 100S.

By SEM, it was observed that the sample 100A (Al_2O_3) showed a more significant presence of particles or conglomerates of 5 nm (Figure 3a), with the predominance of particle sizes between 10 and 30 nm. This morphology has also been observed in catalysts prepared by other authors [38].

The conglomerate's distribution in the 5SA (5 wt% SiO_2) sample shifted from 25 to 50 nm (Figure 3b). When the concentration increased from 5 to 15 wt% SiO_2 (Figure 3c), many 25 nm particle sizes were observed. Moreover, when the concentration increased from 15 to 20 wt% SiO_2 (Figure 3d), a more significant presence of particle sizes between 25 and 150 nm and a lower presence of particle sizes between 200 and 400 nm were observed. Again, when the concentration increased from 20 to 25 wt% SiO_2 (Figure 3e), a bimodal distribution was observed with two maximum values; namely, a set of particles was observed between 25 and 50 nm and another group of particles between 100 and 400 nm. These results indicate that more SiO_2 addition in Al_2O_3 favors the presence of particles larger than 100 nm.

Crystals of 5–12 μm were observed (Figure 3f) when the SiO_2 concentration was 100%. Additionally, a crystal of 100 wt% SiO_2 was observed on the scale of 100 nm ($\times 50,000$) that corresponds to a very compact and continuous structure (not shown), with sharp vertices and huge particle sizes, very different from what was observed in the mixtures of SiO_2 – Al_2O_3 .

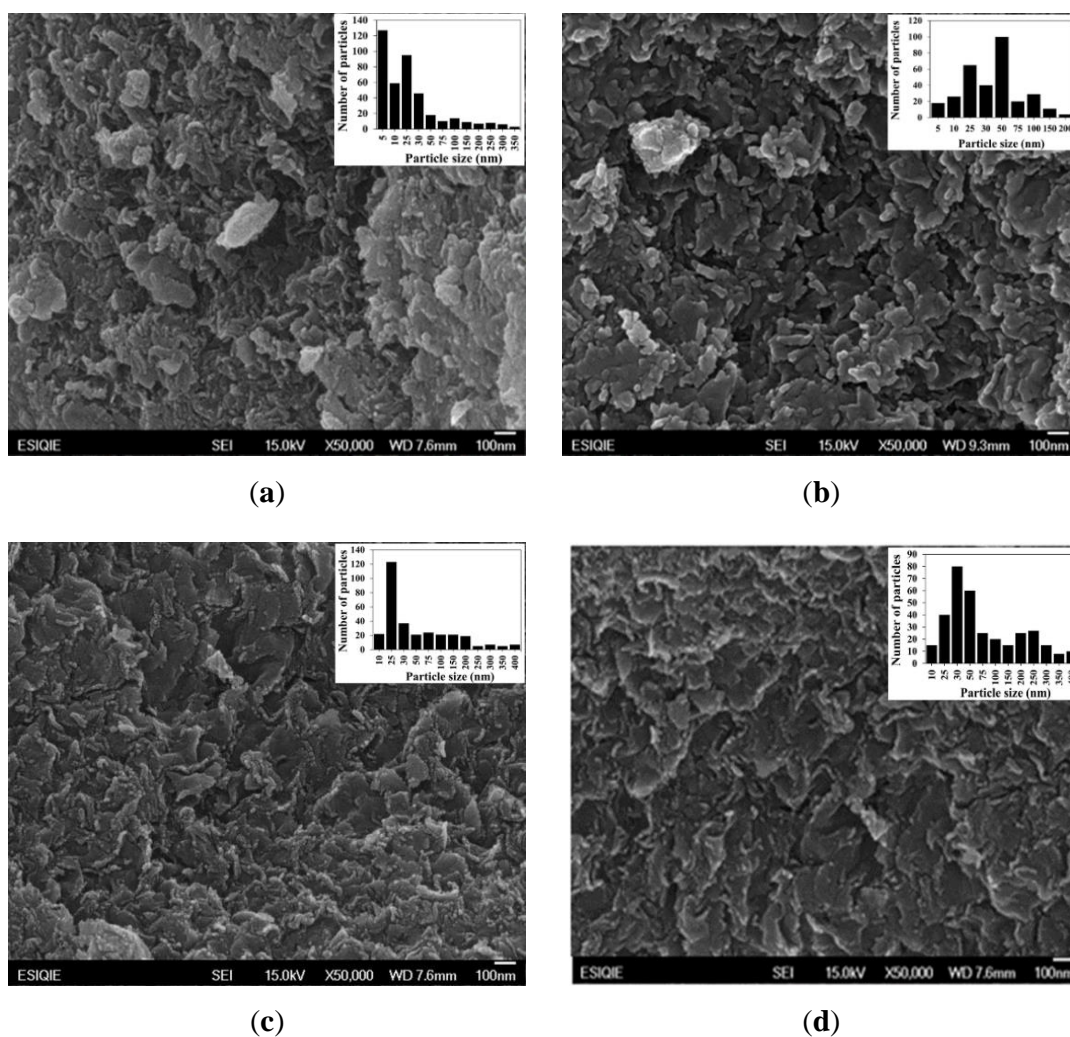


Figure 3. Cont.

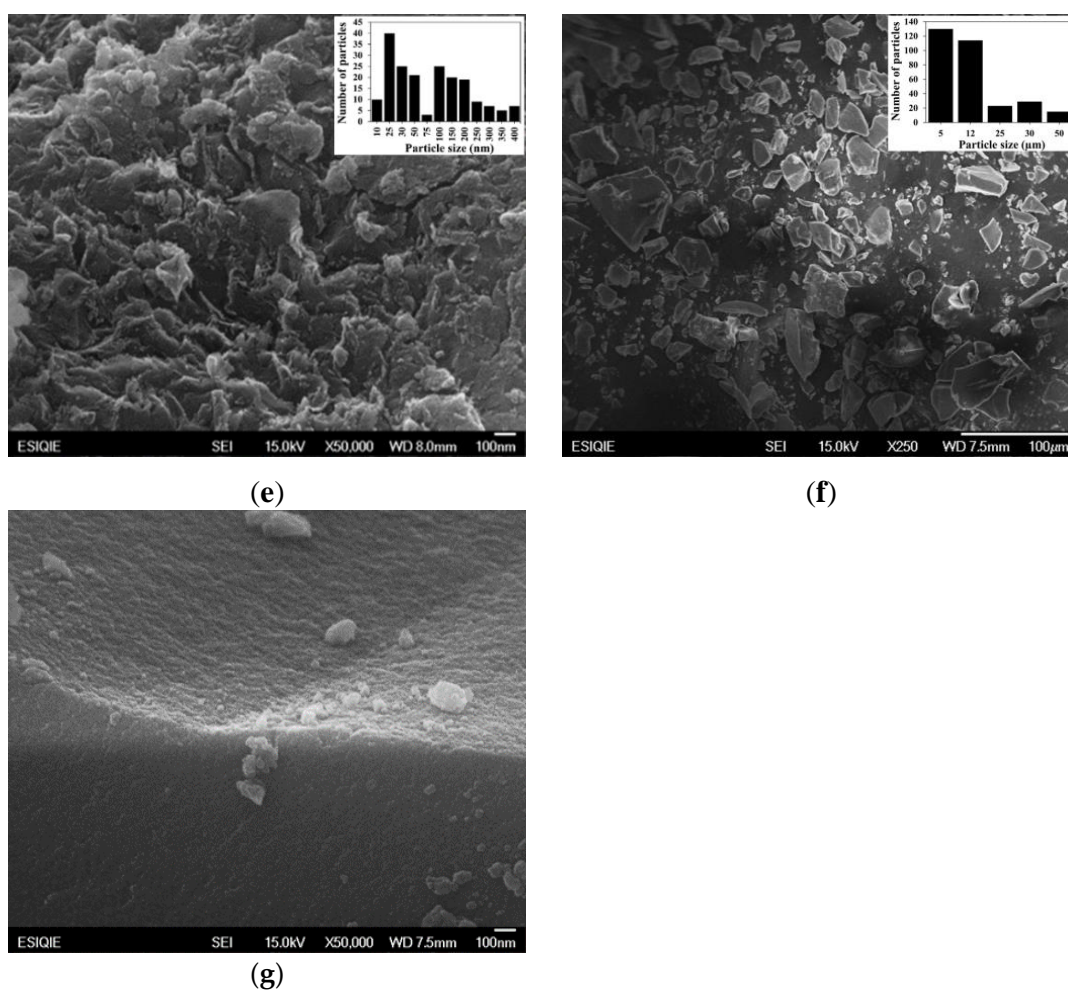


Figure 3. SEM images of $\text{SiO}_2\text{-Al}_2\text{O}_3$ oxides calcined at $550\text{ }^\circ\text{C}$: (a) 100A, (b) 5SA, (c) 15SA, (d) 20SA, (e) 25SA, (f) 100S (resolution $100\text{ }\mu\text{m}$), and (g) 100S (resolution 100 nm).

2.4. Effect of the W Content on the BET Area of the 25SA- WO_x Microspheres

The addition of small amounts of W to the microspheres of the order of 0.5% by weight, called 25SA-0.5 WO_x , reduced or inhibited the loss of the BET-specific area that occurred when the calcination temperature increased from $550\text{ }^\circ\text{C}$ to $950\text{ }^\circ\text{C}$ (Figure 4). The samples without W (0 wt% W) showed a decrease in the area of 7.25% at $550\text{ }^\circ\text{C}$, 26.6% at $650\text{ }^\circ\text{C}$, 41% at $750\text{ }^\circ\text{C}$, and 66% at $950\text{ }^\circ\text{C}$ compared to the samples containing W.

The effect of the thermal stabilization provided by W is maintained when the W concentration increases to 16 wt% W for the samples calcined up to $750\text{ }^\circ\text{C}$ (Figure 4a–c). In comparison, for the samples calcined at $950\text{ }^\circ\text{C}$, this effect is lost at concentrations of more than 8 wt% W (Figure 4d).

2.5. Spray-Dried 25SA Microspheres Obtained with the Straight Rectangular Vanes Disk

The 25SA microspheres produced with the straight rectangular vanes disk (DAR) were mainly spherical particles of different sizes (Figure 5a–d) with few broken particles. In the P1-DAR (Figure 5a) and P2-DAR products or powders (Figure 5b), particles with a diameter up to four times larger than the diameter of the other particles were observed. On the other hand, in the P3-DAR product, the agglomeration or clusters of spherical particles were observed (Figure 5c), and in the P4-DAR product, microspheres of more uniform size were produced (Figure 5d).

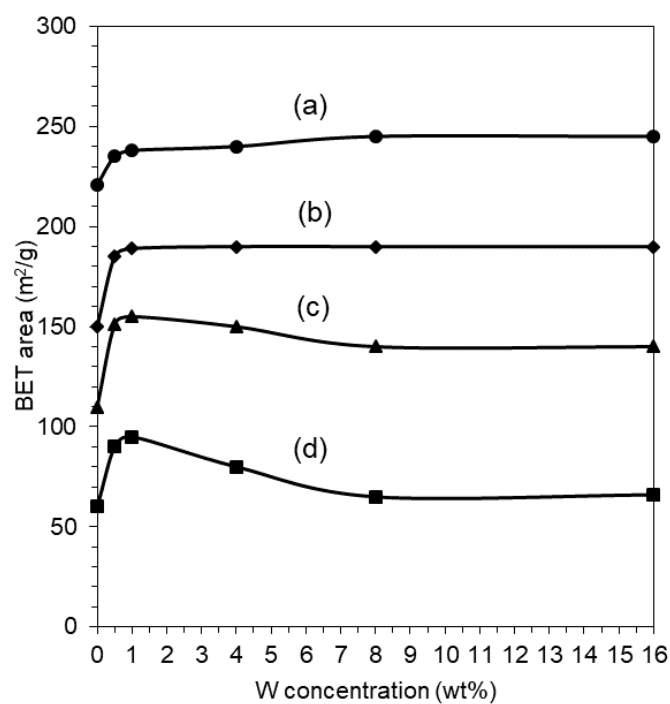


Figure 4. Effect of the W concentration on the BET area of the 25SA-WO_x samples calcined at (a) 550 °C, (b) 650 °C, (c) 750 °C and (d) 950 °C.

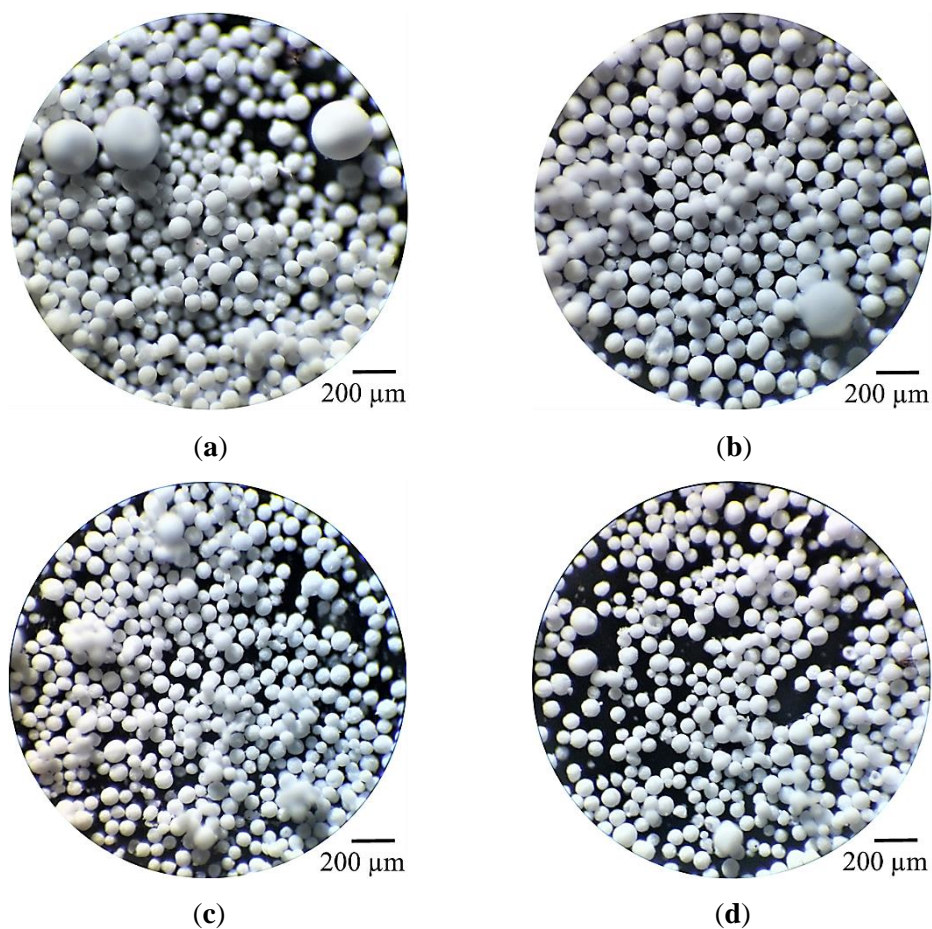


Figure 5. Optical microscopy of the spray-dried 25SA microspheres calcined at 550 °C was obtained with the straight rectangular vanes disk: (a) P1-DAR, (b) P2-DAR, (c) P3-DAR y (d) P4-DAR.

2.5.1. Effect of the DAR-Disk Rotation Speeds on the Particle-Size Distributions (PSD) and the Sauter Mean Diameter (SMD)

When the rotational disk speed (3000 rpm) was decreased, the particle-size distribution (PSD) of the P1-DAR (Figure 6a) product reached its maximum value at a particle diameter of 90 μm , shifting to the right at a larger particle diameter range of 10–230 μm .

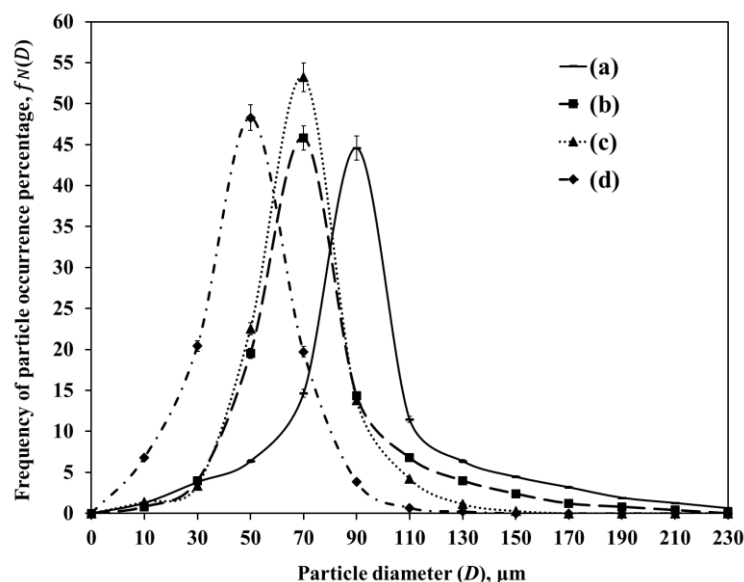


Figure 6. Particle diameter distributions of spray-dried 25SA products calcined at 550 °C, obtained at the following rotational speeds of the straight rectangular vanes disk: (a) 3000 rpm (P1-DAR), (b) 6000 rpm (P2-DAR), (c) 11,500 rpm (P3-DAR), y (d) 14,000 rpm (P4-DAR).

The PSDs of the P2-DAR (6000 rpm) (Figure 6b) and P3-DAR (11,500 rpm) (Figure 6c) products were very similar and slightly skewed to the right, having a maximum value at a particle diameter of 70 μm , with different particle diameter ranges, from 10–230 and 10–150 μm , respectively (Table 2).

Table 2. Physical properties of spray-dried 25SA microspheres calcined at 550 °C.

	Straight Rectangular Vanes Disk				Curved Rectangular Vanes Disk			
	P1-DAR	P2-DAR	P3-DAR	P4-DAR	P1-DAC	P2-DAC	P3-DAC	P4-DAC
Rotation speed of the disc, rpm	3000	6000	11,500	14,000	3000	6000	11,500	14,000
Particle diameter range ¹ , μm	10–230	10–230	10–150	10–130	10–230	10–210	10–170	10–150
Sauter mean diameter (SMD), μm	125	103	79	63	117	101	81	73
Apparent bulk density of powder ² , g/cm^3	0.61	0.63	0.64	0.67	0.64	0.74	0.77	0.79

The percentage of relative error of the measurement of the particle diameters ¹ was $\pm 3.5\%$; while for the bulk density of powder ² was $\pm 4.3\%$.

On the other hand, when the rotational disk speed was increased (14,000 rpm), the PSD of the P4-DAR (Figure 6d) product had its maximum value at the particle diameter of 50 μm and a particle diameter range of 10–130 μm .

The above results indicate that the maximum particle diameter increased as the rotational speed of the atomizer disk decreased. In the work of Huang and Mujumdar [39], they also reported that the maximum particle size of SiO_2 increased when the disk rotation speed decreased.

The Sauter mean diameter (SMD) of the P1–DAR, P2–DAR, P3–DAR, and P4–DAR products or microspheres were 125, 103, 79, and 63 μm (Table 2), respectively. It was observed that increasing the disk rotational speed resulted in a decrease in the particle SMD of the products. This result has also been verified in the works of Filková and Weberschinke [40], Ahmed and Youssef [41,42], and Peng et al. [43], where they also reported that the particle or droplet SMD decreases when the rotation speed of the atomizer disk is increased. From the previous results, it was observed that the P1–DAR and P2–DAR microspheres approach the spherical morphology requirements, as well as the PSD and SMD of the CO combustion promoter support.

2.5.2. Spray-Dried Microspheres of 100A and 25SA with Different W Concentration

Since complete and non-fragmented microspheres were produced with the DAR atomizer, microspheres calcined and delivered from the P2–DAR experiment (6000 rpm) were chosen to prepare the WO_x -containing supports. Measurements of the particle diameter ranges, the SMD, and apparent bulk densities of supports are summarized in Table 3. It can be observed that the minimum particle diameter was approximately 10 μm for all supports, but the maximum particle diameters are a little different. All microspheres approximate the CO combustion promoter support requirements such as PSD, the SMD, and the apparent bulk density of the powder [11,15].

Table 3. Physical properties of the 25SA- WO_x microspheres prepared from the microspheres obtained in the P2-DAR experiment (6000 rpm) and calcined at 550 $^\circ\text{C}$.

	100A ²	25SA–0.5W	25SA–1W	25SA–2W	25SA–4W	25SA–8W	25SA–16W
Particle diameter range ¹ , μm	10–241	10–238	10–240	10–239	10–251	10–254	10–259
Sauter mean diameter (SMD), μm	105	104	106	104	107	109	110
Apparent bulk density of powder ² , g/cm^3	0.63	0.62	0.63	0.62	0.64	0.66	0.69

¹ The percentage of relative error of the measurement of the particle diameters was $\pm 3.5\%$; while for the apparent bulk density of powder² was $\pm 4.3\%$. ² This sample of pure Al_2O_3 was also obtained at 6000 rpm

2.6. Textural Properties of 25SA Microspheres

2.6.1. BET Specific Area

The textural properties of the 25SA microspheres calcined at 550 and 750 $^\circ\text{C}$ are summarized in Table 4. It was observed that by increasing the calcination temperature of the P1–DAR atomizer samples from 550 $^\circ\text{C}$ to 750 $^\circ\text{C}$, the BET area decreased from 227 to 119 m^2/g , respectively, which is to say that the area decreased by 47.6%.

Table 4. Textural properties of the 25SA microspheres calcined at 550 $^\circ\text{C}$ and 750 $^\circ\text{C}$.

Sample	T_C	SSA_{BET} , m^2/g	V_P , cm^3/g	D_P , nm
P1–DAR	550 $^\circ\text{C}$	227	0.40	7.02
P4–DAR		230	0.41	7.17
P1–DAC		233	0.36	6.12
P4–DAC		240	0.36	6.04
P1–DAR	750 $^\circ\text{C}$	119	0.37	12.33
P4–DAR		125	0.38	12.17
P1–DAC		120	0.37	12.34
P4–DAC		129	0.39	11.98

SSA = specific surface area, V_P = pore volume, D_P = average pore diameter, T_C = calcination temperature.

This decrease in the BET area was also observed in the samples obtained with the P1–DAC atomizer ($\approx 48.5\%$). This value was due to the fact that in the microspheres calcined

at 550 °C, an area of 233 m²/g was obtained and, in the samples calcined at 750 °C, an area of 120 m²/g was obtained.

Due to these small differences in BET area, between the geometry of the atomizers, it is likely that there is not a significant effect on the BET area between straight and curved vanes. Instead, the most notable effect on the BET area of the microspheres was the calcination temperature.

Regarding the variation of the pore diameter (D_p), it can be observed that by decreasing the BET area in the microspheres calcined at 550 °C, the D_p increased to almost twice the D_p of the samples calcined at 750 °C, while in the case of pore volume, no significant differences were observed.

2.6.2. N₂ Adsorption–Desorption Isotherms

The N₂ adsorption–desorption isotherms of the calcined 25SA microspheres at 550 °C (Figure 7a) and 750 °C (Figure 7b) exhibited a Type IV isotherm with a type of H2 hysteresis loop, IUPAC classification [44–46], which was characteristic of mesoporous materials [47].

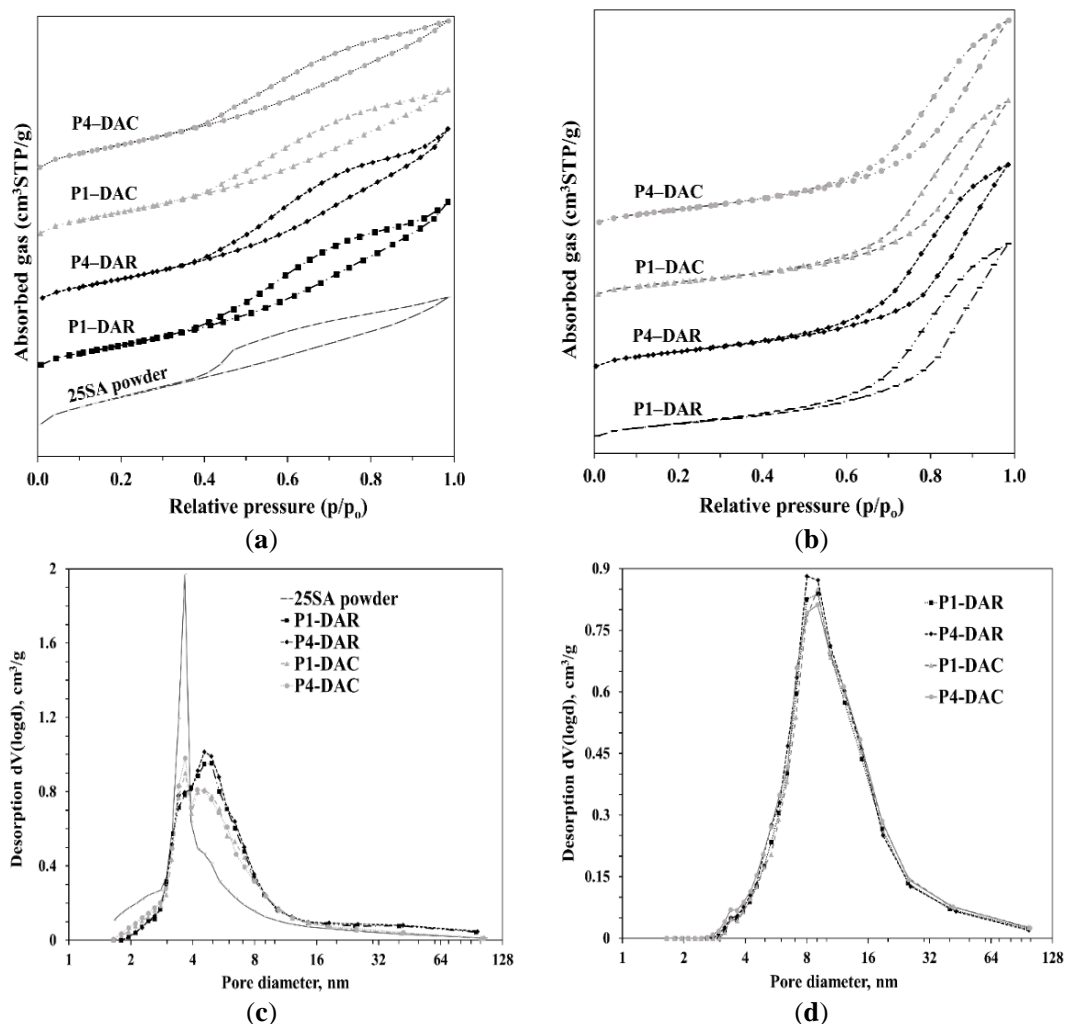


Figure 7. (a,b) N₂ adsorption–desorption isotherms; (c,d) pore diameter distributions of the spray-dried 25SA microspheres calcined at 550 and 750 °C, respectively. The 25SA sample (powder) was the one used for the preparation of the microspheres.

The pore diameter distributions of the 25SA microspheres calcined at 550 °C from the P1-DAR and P4-DAR experiments were mono-modal, with a maximum value in pore diameter of 4.5 nm (Figure 7c), while the P1-DAC and P4-DAC microspheres, calcined at 550 °C, presented bi-modal distributions, with maximum values in the pore diameters

of 3.5 and 4.5 nm, which conserve the maximum values of the distribution of the starting 25SA powder and of the microspheres obtained with the DAR.

In contrast, all the pore diameter distributions of the microspheres obtained with the DAR and DAC atomizers calcined at 750 °C (Figure 7d) were mono-modal, shifted towards a maximum value of pore diameter greater than 8 nm.

2.7. SEM and EDS of Pt/SiO₂-Al₂O₃-WO_x

In Figure 8a, we observed the presence of Pt and the other Al and oxygen atoms, characteristics of the Pt100A catalyst, and its concentration in weight percent. On the other hand, in the Pt25SA-0.5W sample in Figure 8b, we observed the presence of both elements, Pt and W, as well as the Si, Al, and oxygen signals and their concentrations. Finally, in the Pt25SA-4W sample, (Figure 8c) we observed the presence of all the elements—Pt, W, Si, Al and oxygen—and their concentrations.

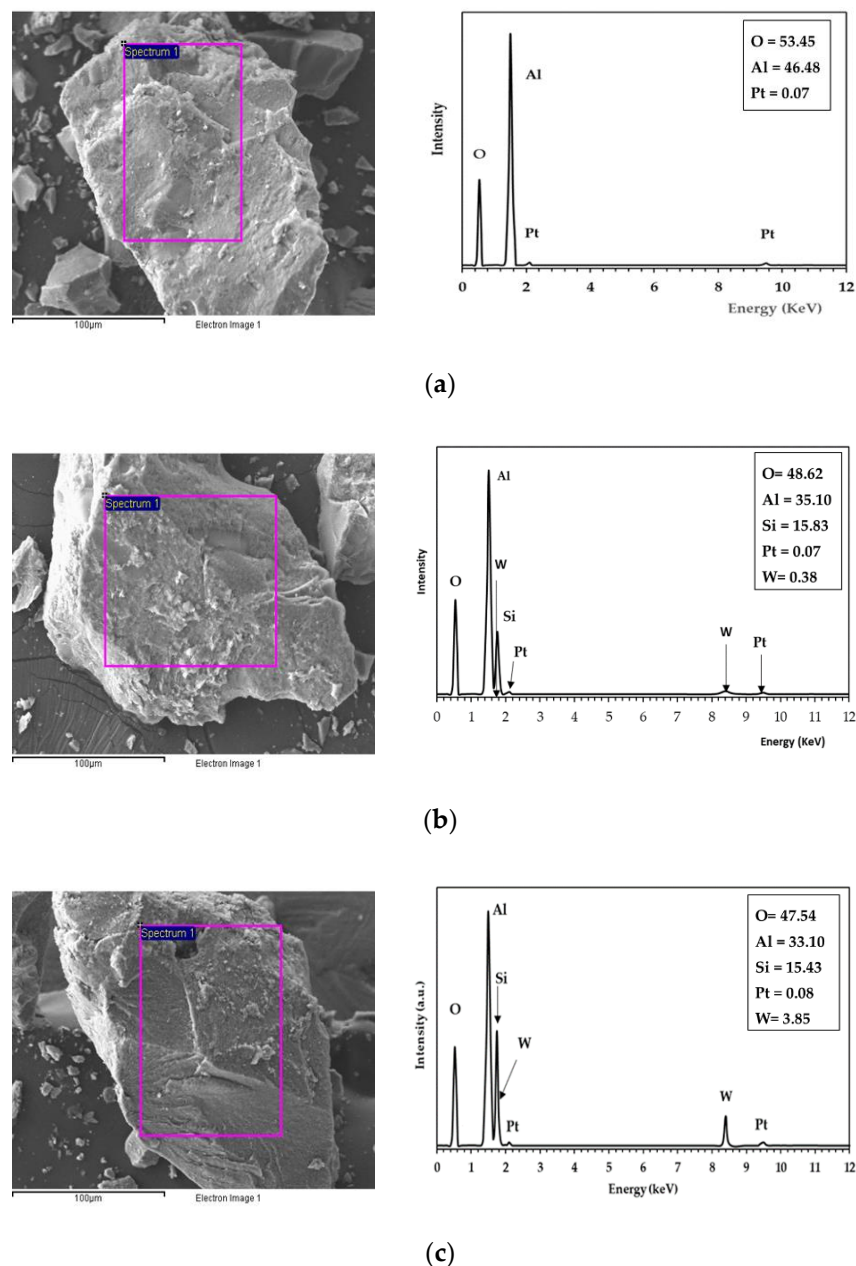


Figure 8. SEM photomicrographs and EDS analysis of the catalysts: (a) Pt100A, (b) Pt25SA-0.5W, and (c) Pt25SA-4W. The composition in weight percent was inserted in the upper inset.

2.8. XRD of the Pt/SiO₂-Al₂O₃-WO_x Catalysts

In order to analyze the interaction of Pt and WO_x by XRD of our catalysts, we carried out the analyzes for the samples Pt25SA-1W of low W content and Pt25SA-16W of high W content (where the concentration of W is slightly above the reported monolayer of 1 atmW/nm² [48]).

The analyzes showed in Figure 9a that at low W content, reflections of W compounds or Pt precursors (PtCl₂) cannot be observed; however, in the case of the sample with high tungsten content (25SA-16W) calcined without Pt (Figure 9b), we could observe that it showed a yellowish color (typical color of WO₃). When this same sample (25SA-16W) was reduced in H₂ by TPR up to 500 °C (Figure 9c), a blue color was observed, typical of bronzes (HTB), either rhombic H_{0.33}WO₃ or cubic H_{0.5} [49].

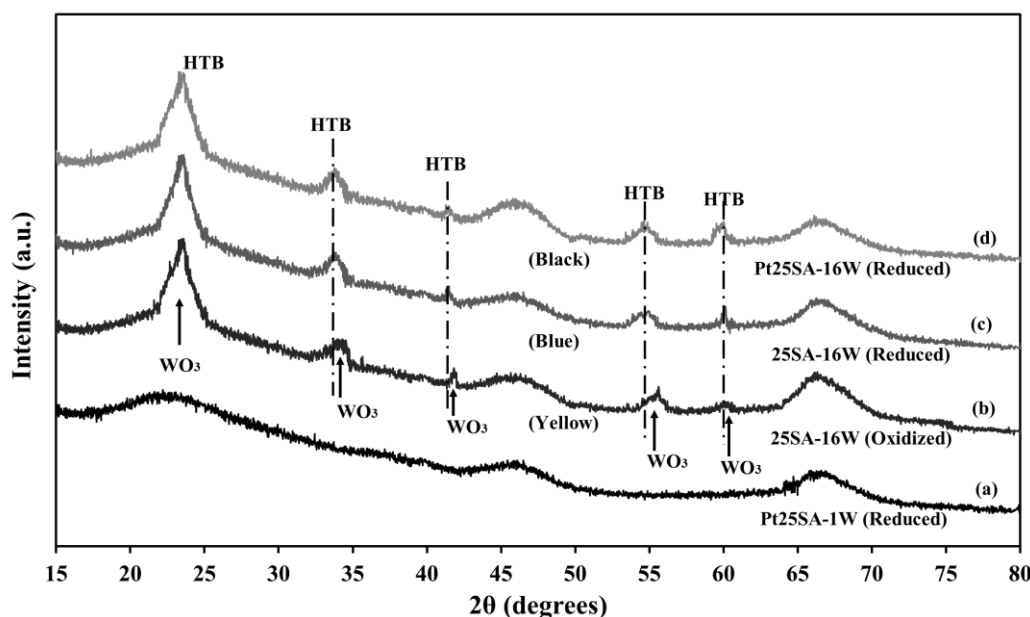


Figure 9. XRD of selected Pt-WO_x samples: (a) Pt25SA-1W reduced gray color, (b) sample calcined 25SA-16W, yellowish color, (c) sample 25SA-16W reduced at 500 °C in H₂, blue color, and (d) Pt25SA-16W catalyst reduced at 500 °C in H₂, black color.

On the other hand, when the Pt25SA-16W catalyst was reduced in the presence of Pt (Figure 9d) at 500 °C, a dark color was found, where no reflections of Pt were observed, (due to the low metal content), but it was possible to observe the change from blue to black that accounted for the formation of metallic Pt and the same formation of the bronzes (HTB).

2.9. TPR of WO_x on SiO₂-Al₂O₃ Microspheres

We observed that the reduction temperatures of WO_x oxides in the absence of Pt are carried out at temperatures greater than 500 °C (Figure 10). It was observed that the temperatures of the maximum peak decrease when the concentration of W decreases, while the starting temperatures in the reduction appear higher as the concentration of W decreases.

These behaviors suggest that the binding energy of O-W increases when there are low concentrations of WO_x below the monolayer in Al₂O₃ (reported monolayer of 1 atmW/nm² [48]) and is weaker when WO_x polylayers are present. During the reduction of these species of mass W oxides of the WO₃ type, the formation of W bronzes (HTB) of the rhombic type H_{0.33} or of the cubic H_{0.5} type has been found [49].

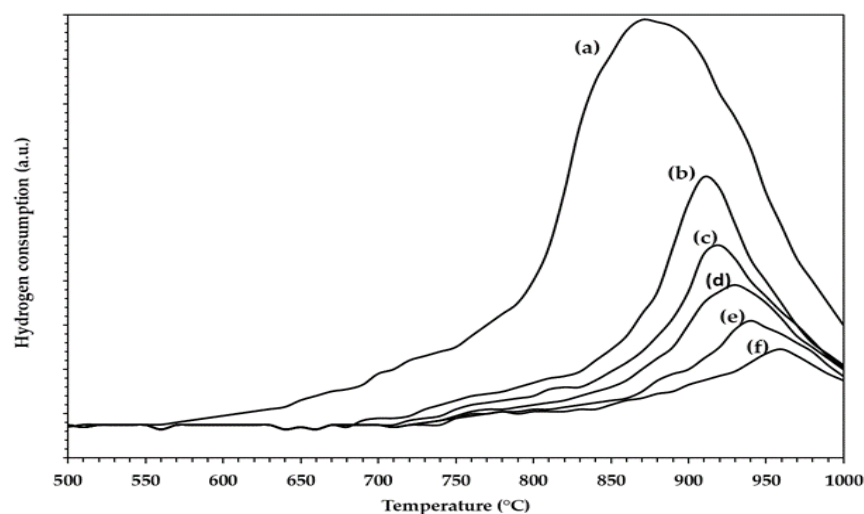


Figure 10. The TPR of $\text{SiO}_2\text{-Al}_2\text{O}_3\text{-WO}_x$ microspheres: (a) 25SA-16W, (b) 25SA-8W, (c) 25SA-4W, (d) 25SA-2W, (e) 25SA-1W, and (f) 25SA-0.5W.

TPR of the Pt/ $\text{SiO}_2\text{-Al}_2\text{O}_3\text{-WO}_x$ Catalysts

The addition of W oxides in the catalysts (Figure 11b–e) did not modify the maximum reduction temperature observed in the TPR analysis of the Pt catalyst without W; however, a decrease in H_2 consumption was observed as the W concentration increased (Figure 11b–e).

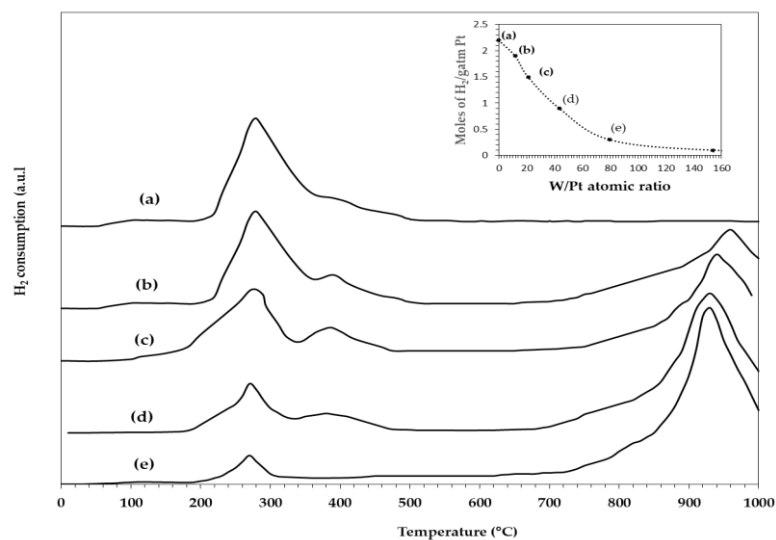


Figure 11. TPR of the Pt/ $\text{SiO}_2\text{-Al}_2\text{O}_3\text{-WO}_x$ catalysts: (a) Pt100A, (b) Pt25SA-0.5W, (c) Pt25SA-1W, (d) Pt25SA-2W, and (e) Pt25SA-4W. The graphic of the H_2 consumption from the TPR (up to 500 °C) of the catalysts is inserted in the upper inset.

In the Pt/ Al_2O_3 catalyst (Pt100A), three reduction peaks were detected with maximums at 115, 270, and 430 °C (Figure 11). These same peaks were observed by other authors when they used Al_2O_3 (Ketjen) in the preparation of their Pt catalysts [50]. The first H_2 peak at 115 °C corresponded to the reduction of mass PtO_2 weakly bound to the support [51,52].

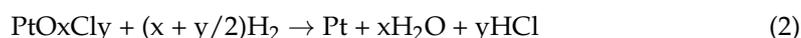
The second reduction peak with a maximum at 245 °C has been attributed to the reduction of a platinum oxychlorinated compound of the type $[\text{Pt}(\text{OH})_x\text{Cl}_y]_n$ when the catalyst has been calcined at 300 °C [50,51] or another Pt oxychloro-complex of the type $[\text{PtO}_x\text{Cl}_y]_n$ that appears at 290 °C, provided the sample is calcined at 600 °C [53].

Other authors, such as Yao et al. [51], proposed the existence of two possible oxidized states of Pt: a particulate phase of PtO_2 reducible at a low temperature and a dispersed

phase of Pt oxide firmly bound to the support that is reduced at a temperature close to the reduction of the previously mentioned Pt oxychloro-complex. According to these authors, the smaller the concentration of platinum oxides, the stronger the interaction of dispersed Pt oxide with Al₂O₃.

Other authors mention the existence of a reduction complex of the Pt–Al₂O₃-*x* type or the formation of the Pt₃Al alloy suggested by Dautzenberg et al. [54]. However, due to our chlorine analysis studies, the proposal by Lieske et al. [53] is more acceptable.

The third peak appeared at 430 °C, corresponding to a Pt species strongly bound to the support. This peak has been reported in other studies [50] and could be related to the formation of another complex of the PtO_xCl_z type; however, a well-defined peak was not found at this temperature in Al₂O₃. When H₂PtCl₆ is impregnated on SiO₂, three peaks are found due to the chlorinated Pt compounds, with the highest at 452 °C [55]. The reduction reactions could be:



It should be noted that Pt compounds containing Cl[−] are more difficult to reduce than Pt compounds containing O[−] or OH[−] groups, and Pt compounds containing low concentrations of Cl[−] are more difficult to reduce [55].

The total sum of the H₂ consumption by TPR for the Pt/Al₂O₃ catalyst (Pt100A) reached a ratio of 2.2 moles of H₂/Pt atom (Figure 11). This value corresponds to a platinum valence of +4, as reported in the literature [51,53].

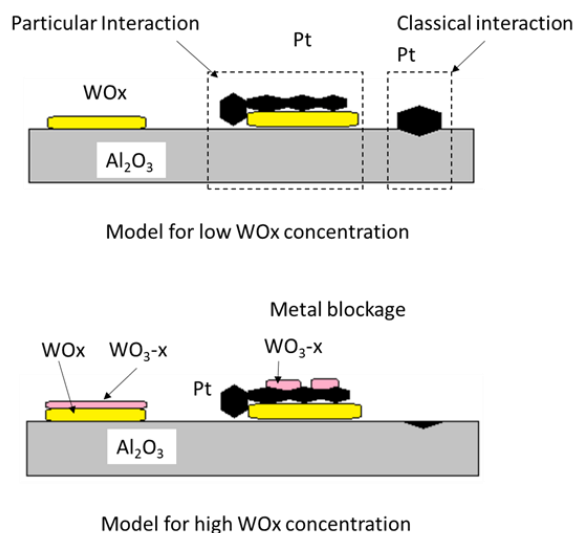
The cause of the decrease in H₂ consumption between (25–500 °C), when WO_x concentration increases, has been reported as a strong interaction of Pt and WO_x precursors by M'Boungou et al. [56]. These authors found that the W species are strongly anchored on the Al₂O₃ support in the presence of the precursors of Pt and W at low concentrations of W (5 wt%). In this case, the W+6 species are not reducible at low temperatures (less than 500 °C), as we have already verified (Figures 10 and 11).

These authors found by TEM that their low W content catalysts composed of 5wtPt–5 wt% W/Al₂O₃ showed an average particle diameter of 16 Å, while the catalysts with a higher W content (5 wt% Pt–35 wt% W Al₂O₃) showed average sizes of 60 Å. The authors explained that the increase in particle size could be due to the presence of weak interactions between Pt and the support, for example, with SiO₂. W could act as a poison or as a moderator blocking the activity of the Pt. In this case, it would be between the Pt and the support. The dispersion and the surface composition of the catalysts can be affected by the diffusion of precursors through the surface of the support, as mentioned by the Ruckenstein–Pulvermacher model of crystallite migration [57].

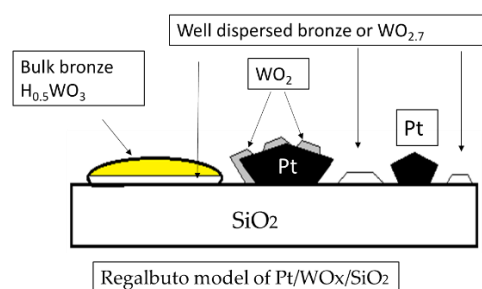
These same authors, in a second publication by M'Boungou et al. [58] by XPS studies, concluded that the W species are strongly anchored on the support in Pt–WO_x/Al₂O₃ catalysts at low W concentrations and are not reducible with an oxidation state of +6 and are not catalytically accessible; W is hampered by small Pt particles. In the case of large W loads, beyond the monolayer on the support, a fraction of W species could migrate to the surface and could be reduced. This fraction of the WO_x species, reduced and large Pt particles, is accessible on the surface, but another fraction of the W species strongly anchored on the support remains inaccessible and non-reducible. See Scheme 1 of the model for low and high WO_x concentration.

The strong interaction of Pt chlorocomplexes (PtCl₂) with WO_x has also been reported by Regalbuto et al. [49]. These authors studied the Pt/WO_x/SiO₂ system using X-ray diffraction (XRD), selective CO chemisorption, and X-ray photoelectron spectroscopy (XPS). It was found that the presence of WO_x decreased final Pt crystallite size, in part by reducing the formation of bulk “Pt-Cl, precursor”. However, CO chemisorption was suppressed; this indicates strong metal-promoter interactions. Changes in Pt electron binding energy suggest that charge transfer may also take place. A model of the surface consisting of Pt crystallites decorated by partially reduced WO_x has been proposed (Scheme 2). This

morphological model was supported by XRD and XPS results which revealed a surface-localized phase of partially reduced WO_x , (likely WO_2). Decoration was also indicated in the trend of XPS Pt/Si ratios.



Scheme 1. M'Boungou et al. [58] model for low and high WO_x concentration in $\text{Pt-WO}_x/\text{Al}_2\text{O}_3$ catalysts.



Scheme 2. Schematic representation of the most probable morphological configuration of the various phases on the $\text{Pt/WO}_x/\text{SiO}_2$ catalysts from Regalbuto et al. [49].

Another work where this same phenomenon of inhibition of WO_x species has been observed in the reduction of metal oxide to noble metal is in the $\text{Ir}/\text{Al}_2\text{O}_3\text{-WO}_x$ catalysts, carried out by Park et al. [59]. These authors prepared several iridium catalysts, keeping the concentration of Ir (1.2 wt% Ir) constant and varying the concentration of W from 0 to 32 wt% W. They showed how the adsorption of CO in Ir of the reduced catalysts decreases as the concentration of WO_x increases, which is very similar to our results.

2.10. Dispersion of the Pt on the Pt/25SA-WO_x Catalysts

The Pt catalyst without W (Pt100A), reduced to 500 °C showed a dispersion of 61%, (Figure 12a) and after reduction at 800 °C, the Pt dispersion decreased to 43% (see the arrow in the Figure 12), suggesting that the Pt particles were sintered. The decrease in the dispersion of the Pt also occurred with the addition of WO_x to the catalyst (or the increase in the atomic ratio W/Pt). This effect has already been reported previously [29,30,60].

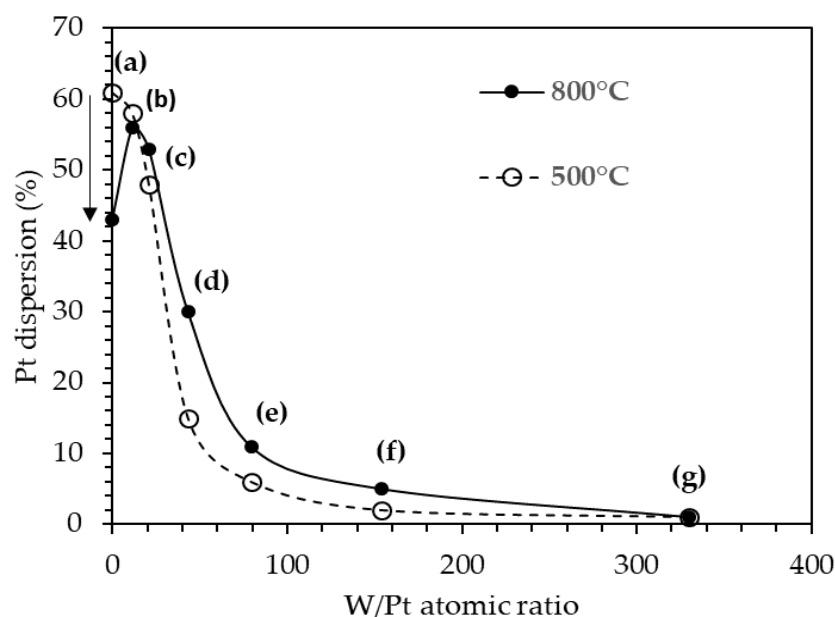


Figure 12. Pt dispersion of the catalysts: (a) Pt100A, (b) Pt25SA–0.5W, (c) Pt25SA–1W, (d) Pt25SA–2W, (e) Pt25SA–4W, (f) Pt25SA–8W, and (g) Pt25SA–16W, reduced to 500 and 800 °C.

In the case of the Pt25SA–0.5W catalyst (Figure 12b) with low W content ($W/Pt = 11.6$) and reduced at 800 °C, a dispersion of 56% was observed, and the same catalyst reduced at 500 °C also showed a similar dispersion of 58%, which contrasts with the dispersion of 43% of the Pt100A catalyst without W reduced at 800 °C. This effect showed the stabilizing effect of WO_x .

For the case of the catalyst Pt25SA–1W (Figure 12c) with a ratio $W/Pt = 20$ and reduced at 800 °C, a dispersion of 53% was observed, while the same catalyst reduced at 500 °C showed a dispersion of 48%, which is still higher than that of the Pt catalyst without WO_x .

As the W/Pt ratio increases (W/Pt ratio > 39), the Pt dispersion strongly decreases at both reduction temperatures, and it was observed that this trend is more pronounced in samples reduced to 500 °C than in samples reduced to 800 °C.

This behavior suggests that the WO_x (or W^{+6} ions) in the presence of PtO_xCl_y could inhibit the formation of metallic Pt because a higher reduction temperature (1000 °C) would be required to obtain Pt crystallites.

This behavior could be explained based on the work of Alexeev et al. [61]. They found, using EXAFS spectroscopy, the presence of metal–metal contributions of Pt and W with oxygen atoms of the γ - Al_2O_3 support. The authors suggest the presence of Pt “clusters” that are stabilized in a highly dispersed state by their interactions with the W cations, which are held in place by interactions with the support through the surface oxygen atoms. In their work, the authors showed that the Pt clusters chemisorbed CO and H_2 and showed activity in the hydrogenation of toluene. They found that the proximity of Pt and W atoms during their preparation determined whether or not they had the ability to enact chemisorption of CO and H_2 .

The stabilizing effect of WO_x on Pt crystals was observed mainly at low W contents (0.5 and 1 wt% W); however, when the concentration increases to more than 2 wt% W, the effect is inverse; that is, the dispersion decreases.

2.11. Surface Model

From the results of the BET area as a function of the WO_x concentration (Figure 4), it can be observed that the effect of WO_x thermally stabilizes SiO_2 – Al_2O_3 , as happens in the case of Al_2O_3 [62], where it has been reported that WO_x retard the crystallographic transitions experienced by Al_2O_3 due to heating at high temperatures. This effect is more evident when the calcination temperature increases from 550 °C to 950 °C.

In Figure 4, it can be observed that the BET area did not decrease drastically in the case of the samples that contained low concentrations of W (0.5 to 1 wt%), which shows the stabilizing effect that WO_x contributes to the support of $SiO_2-Al_2O_3$.

On the other hand, it is known that increasing the WO_x concentration in the surface acidity of Al_2O_3 produces a decrease in the population of Lewis sites evaluated by infrared spectroscopy of chemisorbed pyridine [30].

On the other hand, in the $SiO_2-Al_2O_3-WO_x$ surface scenario, the reduction with H_2 by TPR at 500 °C of the Pt (PtO_xCl_y) oxychloro complexes produced (Figure 11), we observed that the presence of WO_x has a decrease in the reduction of these (PtO_xCl_y) towards the formation of Pt^0 (nanoparticles or clusters). It was observed that at low W contents in the Pt100A and Pt25SA-0.5W catalysts, H_2 consumption by TPR was 2.2 to 1.9 mol $H_2/gatmPt$, respectively. These values are close to the value of 2 found in the stoichiometry reduction equation (Equation (2)).

As already mentioned, the Pt dispersions in the catalysts reduced to 500 °C (Figure 12) decreased in the presence of WO_x , probably due to the difficulty of reducing the PtO_xCl_y bound with WO_x , except for the Pt100A catalyst without W (W/Pt ratio = 0) that showed the highest dispersion of 61%.

In TPR experiments of the 16 wt% W/ Al_2O_3 catalyst (Sample 25SA-16W), we found a peak up to 870 °C (Figure 10a); on the other hand, when the W content was small, as in the Sample 25SA-0.5W (Figure 10f), the maximum reduction temperature rises to 960 °C, which shows a strong effect of the support on the reducibility of the WO_x patches.

When we increased the reduction temperature from 500 °C to 800 °C, we observed a slightly greater dispersion of Pt in almost the entire range of atomic ratios W/Pt (Figure 12), with the exception of the Pt catalyst without WO_x (ratio W/Pt = 0), where the Pt has sintered from 61% to 43%.

These results suggest that there is probably a strong interaction between PtO_xCl_y and WO_x that increases as the concentration of WO_x increases.

The fact that a fraction of Pt remains unreduced to metallic Pt could be due to the fact that WO_x oxides could possibly be decorating the Pt oxychlorides or newly formed Pt particles. The studies of TEM and X-ray diffraction patterns by Regalbuto et al. [63] indicate that WO_x are highly bound to Pt precursors.

The surface model that we propose considers the following aspects: (a) the thermal stabilization produced by WO_x on the $SiO_2-Al_2O_3$ support, (b) the stabilization of the reduced Pt particles up to 800 °C, inhibiting sintering, especially in low W contents, and (c) the substitution of Lewis sites of the support by WO_x species that could possibly help to decrease the mobility of Pt particles during reduction up to 800 °C.

Other surface models for this Pt- WO_x catalytic system supported on SiO_2 or Al_2O_3 have been proposed. The Yermakov model [64] suggests the formation of conglomerates or "clusters" of metallic Pt on SiO_2 , which are stabilized by their interaction with low valence W ions bound to the support. Another superficial model has been proposed by Regalbuto et al. [65], which consists of the presence of large and small crystallites located on the support and on the WO_x phase.

The Pt on the tungsten phase decreased the difficulties in reducing WO_x , leading to the formation of partially reduced compounds called "W bronzes" (hydrogen tungsten bronzes HTB) and suboxides of W. WO_x affected the size of Pt crystallite, in part by decreasing the quantity and size of $PtCl_2$ crystallites in bulk that formed after calcination. Suboxides such as WO_2 form a separate phase from W bronzes, which decorate the surface of Pt particles and thus decrease CO chemisorption. In his model, three well-characterized surface phases were reported: Pt particles, WO_2 decorating the Pt particles, and the bronzes (HTB) in a bulk phase.

In another model proposed by M'Bongou et al. [56], the authors proposed the existence of two classes of surface structure: a structure with a low content of W (W < 5wt%) characterized by small particles of Pt, where the activity and selectivity of the catalyst are due to a particular interaction between Pt and WO_x instead of the known classical

interaction of Pt and Al_2O_3 with small Pt particles interacting with the support (which was called classical interaction) and the interaction between Pt° and $\text{W}^{6+}/\text{Al}_2\text{O}_3$, which was called particular interaction and another surface part of W^{6+} separately. The other structure, with high content of W (where the concentration of $\text{W} > 18$ wt%), consisted of metallic Pt and tungsten with various oxidation states from +6 to 0. W^{6+} could be a tungstate strongly anchored to the support, and a part of Pt could have W with low oxidation states produced by the reduction of a fraction of WO_x that migrates in the upper part of the Pt particles.

Our model (Figure 13) has been built with the results of our characterizations and has taken into account the aforementioned models in both SiO_2 and Al_2O_3 . The Pt catalyst without WO_x (Pt100A) is shown in Figure 13a, wherein the absence of WO_x produces Pt sintering when we reduce the temperature from 500 °C to 800 °C. When a small amount of W is added to the Pt25SA–0.5W catalyst (Figure 13b) a phenomenon of stabilization of Pt particles is observed; the sintering is inhibited due to the obstruction of WO_x , with which an increase in the dispersion of Pt with respect to the previous case could be presented. By further increasing W in the Pt25SA–1W catalyst, the stabilization and reduction of the Pt oxychlorocomplexes to Pt particles was also observed (Figure 13c,d). In the catalysts with a higher concentration of W (4 to 16wt%W), the reduction of PtO_xCl_y was complicated to carry out.

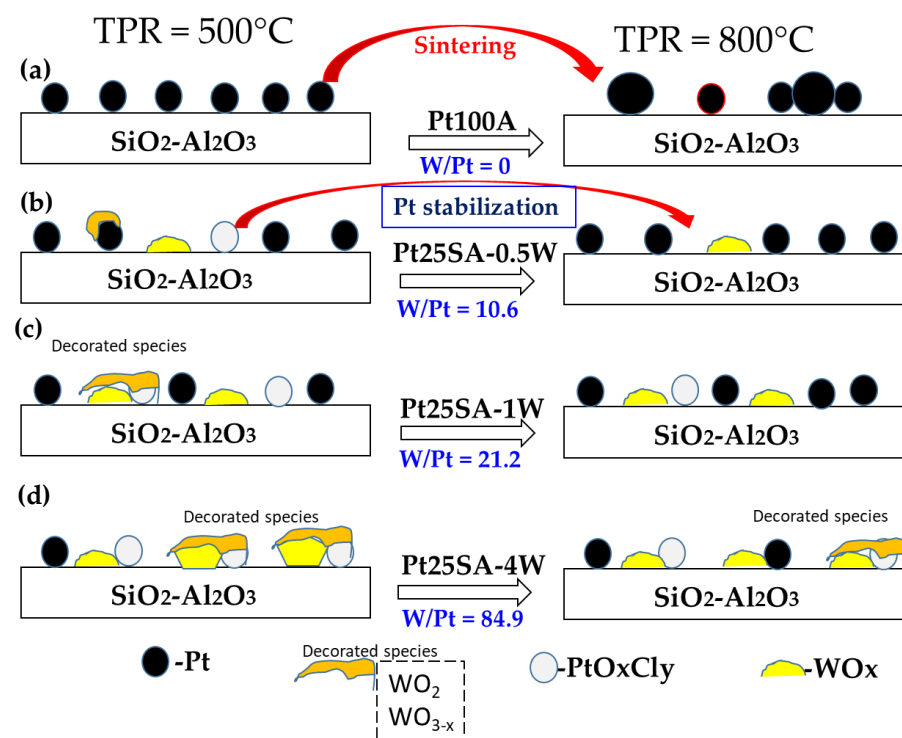


Figure 13. Surface model of the Pt/ SiO_2 – Al_2O_3 – WO_x catalysts: (a) Pt100A without WO_x , (b) Pt25SA–0.5W, (c) Pt25SA–1W, and (d) Pt25SA–4W.

2.12. CO Combustion

The conversion of CO followed a typical light-off process during combustion on the active sites of Pt (Figure 14). As is known to occur at a low temperature, the reaction was self-inhibited due to the high coverage of the active sites with CO [66,67], and as a consequence, the conversion was low.

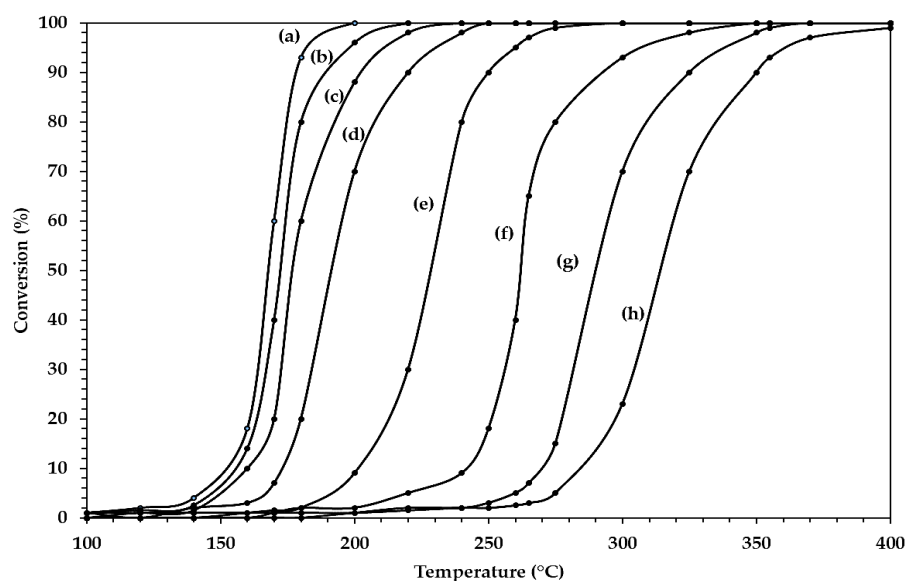


Figure 14. CO conversion of Pt25SA-WO_x catalysts reduced to 800 °C: (a) Pt100A-(reduced to 500 °C), (b) Pt25SA-0.5W, (c) Pt25SA-1W, (d) Pt100A catalyst (reduced at 800 °C), (e) Pt25SA-2W, (f) Pt25SA-4W (g), Pt25SA-8W, and (h) the 25SA support.

On the contrary, at higher temperatures, the conversion of CO was high, while the surface covered with CO was relatively low. It was identified that in this region, the reaction rate was limited by the transport of reactants to the catalytic surface. In the intermediate region of the light-off, the reaction rate increased due to the heat of reaction and the availability of CO, while at a higher temperature the availability of CO was lower. The conversion results of the catalysts against CO combustion temperature (Figure 14 and Table 5) starting at 140 °C are similar to some reported in the literature [38,68].

Table 5. CO combustion temperatures at conversions of 50% (T₅₀) and 90% (T₉₀) for catalysts prepared: Monometallic Pt reduced at 500 °C (Pt100A-(500)) and 800 °C (Pt100A-(800)), bimetallic Pt-W (Pt25SA-0.5W to Pt25SA-8W), and the support 25SA.

Catalyst	T ₅₀ (°C)	T ₉₀ (°C)
Pt100A-(500)	168	180
Pt25SA-0.5W	172	190
Pt100A-(800)	179	203
Pt25SA-1W	191	220
Pt25SA-2W	230	250
Pt25SA-4W	262	290
Pt25SA-8W	290	325
25SA (support)	315	350

In order to compare the catalytic activity of these catalysts, we adopted the temperature at which 50% and/or 90% conversion were reached (T₅₀ and/or T₉₀). From Figure 14a, it can be observed that the Pt100A catalyst (reduced to 500 °C) was the most active catalyst, with a T₅₀ of 168 °C. This value corresponds to a Pt dispersion of 61%.

The following catalyst Pt25SA-0.5W reduced to 800 °C (Figure 14b) showed a T₅₀ of 172 °C, corresponding to a dispersion of 56%. Then the catalyst Pt25SA-1W (Figure 14c) showed a T₅₀ = 179 °C with a dispersion of 53%.

Then the Pt catalyst, the Pt100A catalyst (Figure 14d) reduced at 800 °C, showed a T₅₀ of 191 °C, corresponding to a dispersion of 43%.

In general, the following catalysts kept the following order: the catalyst Pt25SA-2W (Figure 14e) showed a T₅₀ = 230 °C with a dispersion of 30%. Then the catalyst Pt25SA-4W (Figure 14f) showed a T₅₀ = 262 °C with a dispersion of 11%. Then the catalyst Pt25SA-8W

(Figure 14g) showed a $T_{50} = 290$ °C with a dispersion of 5% and finally, the support 25SA showed a $T_{50} = 315$ °C (Figure 14h). These values of catalytic activity relative to T_{50} were consistent with the metal dispersion of Pt.

The conversion of CO in the 25SA support was not significant up to 350 °C, as reported in other works [38].

The conversion of CO (Figure 14) is related to the CO and O₂ adsorption stages. Regarding the thermodesorption of CO in Pt nanoparticles, Gu et al. [68] clearly showed two bands or desorption peaks, which indicated heterogeneity at the adsorption sites, linked to different activation energies in the desorption process. These energies are related to the surface coverage of CO on the surface of Pt where the particle size distribution of Pt has large participation [69]. Given the results of thermodesorption of CO, it was mentioned that the first peak at a low temperature (100–260 °C) is associated with the linear desorption of CO on small particles [68], and the adsorption of CO at a high temperature (300–400 °C) may be due to bridge-bonded CO species [70].

The most marked effect on the combustion of CO is related to the metallic phase of Pt obtained after the reduction at 800 °C; that is to say, the dispersion of Pt showed a strong effect on the conversion, derived from the presence of W oxides at a low concentration (0.5 and 1 wt% W).

We did not find significant differences in the conversions of the catalysts prepared with the microspheres obtained by the two (Pt–DAC and Pt–DAR) atomizers during the CO conversion. On the other hand, it has been reported that catalysts calcined at temperatures below 800 °C were active [38] and also that the noble metal existed in two states of aggregation: clusters (1–3 nm) and larger aggregates (20–100 nm). Additionally, it has been found that the Pt supported without WO_x does not present strong interaction with the support at a high calcination temperature, resulting in three-dimensional Pt nanoparticles.

2.13. Comparison with Other Studies

Studies of the catalytic combustion of CO using Pt show (Table 6) that the catalytic activity depends on several factors, such as the concentration of Pt, the amount of catalyst, and the presence or absence of reducing agents such as H₂.

Table 6. Comparison of CO combustion studies with catalysts containing Pt.

Catalysts	Pt (%)	Calcination (°C, (h))	GHSV (h ⁻¹)	Feed Conc. (vol.%)	Pt Dispersion (%)	T ₅₀ (°C)	T ₉₀ (°C)	Reference
Pt/Al ₂ O ₃	1	550, 450	120,000 ¹	CO-0.2 O ₂ -1.0 NO-0.05 He-balance	-	169	176	Ivanova et al. [38]
Pt/Ce–Zr–SO ₄ ²⁻ Ce/Zr = 4:1	1	500, 3	24,000	CO-0.1 O ₂ -10 NO-0.05 C ₃ H ₆ -0.05 N ₂ -balance	58	175	184	Gu et al. [68]
Pt/Al ₂ O ₃ Sol-gel	2	500, 13	34,286	CO-1.0 O ₂ -1.35 H ₂ -60 CO ₂ -25 H ₂ O-10 He-balance	8.9	100	135	Manasilp and Gulari [71]
Pt/Al ₂ O ₃	1	500, 4 ³	80,000	CO-0.5 O ₂ -10 NO-0.02 CO ₂ -20 H ₂ O-10 He-balance	40	164	176	Akil et al. [72]
Pt/Al ₂ O ₃	0.03	500, 2	2,760,000 ²	CO-6.94 O ₂ -12.97 He-80.09	36	460	475	de Carvalho et al. [6]
Pt/SiO ₂ –Al ₂ O ₃ –WO _x	0.05	550, 6 800, 2 ³	24,000	CO-7 O ₂ -13.5 He-79.5	61	168	179	This study

¹ Estimated value. ² The value of the promoter weight was taken. ³ Reduction conditions.

The effect of the concentration of Pt in the catalyst can be observed in the work of Manasilp and Gulari [71], where they used 2wt% of Pt, and the conversion temperatures of 50% and 90% were the lowest of $T_{50} = 100\text{ }^{\circ}\text{C}$ and $T_{90} = 135\text{ }^{\circ}\text{C}$, respectively. However, this evaluation started from a gas mixture of H_2 , O_2 , and H_2O . The authors found that the presence of H_2O vapor dramatically increases the oxidation reaction of CO, especially at low temperatures. The conversion increased up to 10 times when 10 vol.% H_2O was added.

In our case, we used a concentration of 0.05wt% of Pt, which is much lower than the concentration of Pt used by Manasilp and Gulari [71]; however, it seems clear that the dispersion of Pt is the relevant parameter. The temperature at which we obtained 50% conversion was $168\text{ }^{\circ}\text{C}$, compared to the temperature of $100\text{ }^{\circ}\text{C}$ of the previous work. The difference of $68\text{ }^{\circ}\text{C}$ is not too high considering the low concentration of Pt.

The study by Ivanova et al. [38] is similar to ours in respect to the CO combustion results, and in that, an Al_2O_3 prepared in the laboratory was used. The authors report a T_{50} of $169\text{ }^{\circ}\text{C}$ against a T_{50} of $168\text{ }^{\circ}\text{C}$ in this work. The authors made a very good study of the effect of the calcination temperature of the support and the catalyst. In Pt/ Al_2O_3 catalysts calcined at relatively low temperatures of $550\text{ }^{\circ}\text{C}$ (for Al_2O_3) and $450\text{ }^{\circ}\text{C}$ (for Pt/ Al_2O_3), Pt was present in the form of metal clusters.

Another work similar to ours is that of Akil et al. [72], where they evaluated a catalyst with 1 wt% Pt and a gas mixture containing CO, O_2 , NO, CO_2 , and H_2O . They reported a T_{50} of $164\text{ }^{\circ}\text{C}$, which is close to ours (T_{50} of $168\text{ }^{\circ}\text{C}$).

For their work, Gu et al. [68] prepared a 1 wt% Pt catalyst supported in $\text{CeO}_2\text{-ZrO}_2\text{-SO}_4^{2-}$, where a T_{50} of $175\text{ }^{\circ}\text{C}$ was observed, which is close to ours (T_{50} of $168\text{ }^{\circ}\text{C}$). The authors found that the presence of sulfates (SO_4^{2-}) improves the combustion conversion of CO significantly due to the formation of $\text{Pt}^{\delta+}\text{-(SO}_4^{2-})^{\delta-}$ species, which were very active for the combustion of CO and more resistant to the presence of SO_2 .

Finally, the study by de Carvalho et al. [6] was working with a 0.03 wt% Pt in Al_2O_3 catalyst mixed with a stabilized cracking catalysts. The evaluation was carried out on a solid mixture of 0.005 g of this catalyst with 1.2 g of a used commercial catalyst and balanced from catalytic cracking. The T_{50} temperature was $460\text{ }^{\circ}\text{C}$, a much higher value than the one we reported (T_{50} of $168\text{ }^{\circ}\text{C}$); however, the evaluation is closer to the real conditions of the combustion promoter of the FCC plant and the Pt dispersion they reported was 36%.

3. Materials and Methods

3.1. Preparation of Macro-Spheres of $\text{SiO}_2\text{-Al}_2\text{O}_3$

In this study, macrospheres were prepared from mixtures of $\text{SiO}_2\text{-Al}_2\text{O}_3$ (3 mm) and microspheres (10–230 μm) of $\text{SiO}_2\text{-Al}_2\text{O}_3$ with a fixed composition; the former was used to study mechanical resistance, and the latter made up the main study.

Initially, we started with the synthesis of metasilicic acid (H_2SiO_3), which was obtained in a stirred tank reactor (SAISA, Mexico City, Mexico) from an aqueous solution of 34.45 kg of sodium silicate Na_2SiO_3 (Silicatos Especiales, Ecatepec de Morelos, México), with a pH of 9.5, by precipitation with 5.24 L of HCl at 32 wt% (± 0.2 wt%) (Acimex, Mexico City, Mexico), using phenolphthalein as an indicator. The gel derived from the polymerization reaction was continuously stirred at $25\text{ }^{\circ}\text{C}$ until it obtained a pH of 2.5 (± 0.1) with a pH meter (Conductronic, Puebla, Mexico). The gel was left to rest for 48 h at $25\text{ }^{\circ}\text{C}$ for the formation of the crystals and their aging. Subsequently, the gel was washed in a centrifuge with demineralized water until a pH of 4.5 was obtained, and it was left to rest for 48 h.

The boehmite gel [$\text{AlO}(\text{OH})$] was obtained from a solution of 37 kg of $\text{Al}_2(\text{SO}_4)_3$ (Alquimia, Mexico City, Mexico) in 20 L of H_2O de-ionized by precipitation with 25 L of a 38 wt% (± 0.5 wt%) NH_4OH solution (Acimex, Mexico) at $60\text{ }^{\circ}\text{C}$ in an intermittent stainless steel reactor (SAISA, Mexico). The gel derived from the reaction was continuously stirred until a pH of 8.5 (± 0.1) was obtained. The precipitate was allowed to stand at $25\text{ }^{\circ}\text{C}$ for 72 h for crystal growth and gel aging. The filtered gel was washed 5 times in a centrifuge with demineralized water until a pH of 7.2 (± 0.1) was obtained, and it was left to rest for 48 h.

The H_2SiO_3 and $\text{AlO}(\text{OH})$ gels were mixed in calculated amounts to obtain the SiO_2 – Al_2O_3 solids and shaken on an orbital shaker (Thermo Scientific, Max, Waltham, MA, USA) for 1 h at 120 rpm. The SiO_2 – Al_2O_3 macrospheres were dried in a rotary drum dryer to obtain a diameter between 3–5 mm in such a way that 3 mm spheres were obtained by calcination.

The macrospheres had the composition shown in Table 7: 100wt% Al_2O_3 (100A), 5wt% SiO_2 –95wt% Al_2O_3 (5SA), 10wt% SiO_2 –90wt% Al_2O_3 (10SA), 15wt% SiO_2 –85wt% Al_2O_3 (15SA), 20wt% SiO_2 –80wt% Al_2O_3 (20SA), 25wt% SiO_2 –75wt% Al_2O_3 (25SA), and 100wt% SiO_2 (100S). The samples named 100A and 100S corresponded to the pure $\text{AlO}(\text{OH})$ and H_2SiO_3 gels, respectively.

Table 7. Composition of the SiO_2 – Al_2O_3 macrospheres calcined at 550 °C.

Sample	wt% SiO_2 ¹	wt% Al_2O_3 ²	pH ± 0.1
Al_2O_3 com.	0	100	8.2
100A	0	100	8.5
5SA	5.7	94.3	8.1
10SA	11.8	88.2	7.6
15SA	15.9	84.1	7.2
20SA	17.6	82.4	6.8
25SA	25.5	74.5	6.4
100S	100	0	4.5

^{1,2} Absolute errors of the SiO_2 and Al_2O_3 content in the mixtures were ± 1.3wt% SiO_2 and ± 1.1wt% Al_2O_3 .

For comparison, alumina macrospheres (Al_2O_3 com.) with a diameter of 3 mm were also prepared. For this purpose, a mixture of 1 kg of commercial hydrated alumina powders (QR Minerals, Querétaro, Mexico), 30 g of polyvinyl alcohol (Merck, Naucalpan de Juárez, Mexico), and 200 mL of demineralized water were used, later forming the spheres in a rotary drum dryer. Finally, all the spheres were dried at 120 °C for 48 h and then calcined from 25 °C to 550 °C (heating rate of 2 °C/min), keeping the macrospheres at 550 °C for 6 h.

Subsequently, the calcined spheres were subjected to tests under axial compression to evaluate their resistance to rupture, utilizing a universal mechanical testing machine (United, Model SSTM-1) with a load cell of 10 kN and a controlled-load speed of 0.05 cm/min (relative error of ±0.1%). Each evaluation was carried out in triplicate.

3.2. Formation of Fines by Attrition Using the Jet-Cup Technique

The weight percentage of fines (<20 µm) contained in some of the microspheres showed in Table 1 was measured by weight difference before and after the jet-cup attrition tests. The jet-cup test system was based on a design proposed by ASTM [32] consisting of an air inlet tube connected to the sample cup at the bottom, a sedimentation chamber, and a fine-capture filter at the top. The details and geometric dimensions of the equipment have been described [32]. A sample of 5 g was loaded into the sample cup and then attached to the settling chamber for all jet-cup tests. Afterward, an airflow of 20 L/min was introduced, which was introduced tangentially and before passes through a humidifier. The temperature and relative humidity of the air were 20 °C and 53%, respectively, with an attrition time of 1 h. At the end of each test, the fines were recovered in the upper filter, and the coarse particles in the sample cup would later be mixed with them to measure the percentage of fines generated.

3.3. Preparation and Rheology of the 25SA Suspension for Spray Drying

For the formation of microspheres by spray drying (Appendices A and B), a feed suspension was prepared, composed of 43 ± 0.5 wt% of the 25SA powder sample (25wt% SiO_2 –75wt% Al_2O_3), 55.5 ± 0.5 wt% demineralized water, 1.3 ± 0.01 wt% of polyvinyl alcohol (Merck, Mexico), as a binder, and 0.2 ± 0.01 wt% of ethylene glycol (Merck, Mexico), as plasticizer [73–76]. The density of the suspension was 1.47 ± 0.06 g/cm³. This suspension was used in the spray drying experiments, using two atomization discs with vanes of dif-

ferent geometry to meet the PSD requirements and the particle SMD of the CO combustion promoter support used in the FCC units [11,13,15].

Additionally, alumina microspheres (100A) were prepared by spray drying using the same procedure as above that was used with the 25SA powder. The suspension was atomized with the straight rectangular blade disc (DAR) with a rotation speed of 6000 ± 121 rpm.

The rheological parameters of the 25SA suspension were determined with a commercial rheometer (Anton Paar, MCR 502) equipped with a sample temperature control system and an EC-motor in combination with the low-friction air bearing. A parallel plate geometry with a diameter of 25 mm was used, fitting a sample thickness of 1 mm between the parallel plate and the sample holder. The temperature of the sample in the determination was 20 ± 1 °C. The cutting speed was controlled in the range of 0.1 to 100 s^{-1} . The measurement was carried out three times to verify the reproducibility of the results.

3.4. Impregnation of WO_x and Pt in the Microspheres

Derived from the study of mechanical resistance of the SiO₂–Al₂O₃ microspheres (Figure 1), the mixture 25SA (25wt%SiO₂–75%Al₂O₃) was chosen as the one with the highest mechanical resistance to rupture, preserving the presence of the Lewis acid sites of the Al₂O₃ and an appropriate BET area to deposit both WO_x and Pt. The microspheres selected for the impregnation of Pt and W were those obtained from the P2–DAR experiment (6000 rpm), and they were calcined at 550 °C. The Sauter diameter (SMD) was 103 μm.

To exchange the W oxides in the 25SA microspheres, a solution of (NH₄)₁₂W₁₂O₄₀·5H₂O (Aldrich, Saint Louis, MO, USA) with a concentration of 7.68×10^{-3} M (as W) was used to carry out an impregnation on the microspheres of SiO₂–Al₂O₃. A change in pH was observed from 6.5 until it equilibrated at 8.7 after 20 min. The change in pH was due to an exchange of tungstate ions with the hydroxide groups of Al₂O₃ and is supported by micro-electrophoresis and potentiometric titration studies by Karakonstantis et al. [77]. Microspheres with different contents of W promoter were dried at 110 °C for 24 h, then calcined at 550 °C for 4 h to finish forming the structural promoter of WO_x [30] (Table 8).

Table 8. Composition of the 25SA–WO_x microspheres calcined at 550 °C.

Sample	wt% SiO ₂	wt% Al ₂ O ₃	wt% W ¹
25SA–0.5W	25.69	73.81	0.501
25SA–1W	25.56	73.443	0.997
25SA–2W	25.30	72.692	2.008
25SA–4W	24.783	71.219	3.998
25SA–8W	23.745	68.246	8.009
25SA–16W	21.697	62.312	15.991

¹ The absolute error of the W content in the microspheres was $\pm 0.005\text{wt}\%$. The W content in the microspheres was estimated by atomic absorption spectroscopy.

The nominal impregnation of 500 ppm of Pt or 0.05wt% Pt in the microspheres 100A and 25SA–WO_x was carried out by the incipient wetness impregnation method using a beaker stirred at 60 °C. Measurements of 5 g of microspheres and 6.6 cm³ of an H₂PtCl₆ solution (Aldrich, USA) were impregnated for 2 h with a concentration of 0.38 mgPt/cm³ until reaching a pH of 6 and evaporating the moisture. Afterward, the samples were dried in an oven at 120 °C for 48 h and finally calcined in a muffle at 550 °C for 6 h. These catalysts were reduced in the presence of 30 cm³/min H₂ gas flow at 500 °C and 800 °C for 2 h, respectively. Catalysts reduced up to 800 °C were evaluated in the combustion of CO.

The microspheres 100A, 25SA–0.5W, 25SA–1W, 25SA–2W, 25SA–4W, 25SA–8W, and 25SA–16W with deposited Pt were named: Pt100A, Pt25SA–0.5W, Pt25SA–1W, Pt25SA–2W, Pt25SA–4W, Pt25SA–8W, and Pt25SA–16W, respectively (Table 9).

Table 9. Composition (wt%) of the Pt25SA–WO_x catalysts calcined at 550 °C.

Sample	wt% SiO ₂	wt% Al ₂ O ₃	wt% W	wt% Pt ¹	W/Pt (Atom/Atom)
Pt100A	0	99.946	0	0.0538	0
Pt25SA–0.5W	25.680	73.760	0.504	0.0554	11.60
Pt25SA–1W	25.553	73.409	0.982	0.0561	20.066
Pt25SA–2W	25.287	72.646	2.012	0.0549	39.02
Pt25SA–4W	24.789	71.218	3.950	0.0426	98.34
Pt25SA–8W	23.760	68.165	8.030	0.0445	191.38
Pt25SA–16W	21.835	62.550	15.57	0.0467	353.6
Pt–DAR	25.857	74.100	0	0.0430	0
Pt–DAC	25.747	74.210	0	0.0439	0

¹ The absolute error of the Pt content in the microspheres was ± 0.0064 wt% Pt. The Pt content in the microspheres was estimated by atomic absorption spectroscopy.

In order to observe the effect of the geometry of the vanes of the atomization discs on the combustion of CO, the Pt–DAR and Pt–DAC catalysts were prepared. The first was prepared using the microspheres from the P2–DAR experiment (6000 rpm), and the second was prepared using the microspheres from the P2–DAC experiment (6000 rpm).

The quantitative analysis of Pt and W in the catalysts was carried out in atomic absorption equipment (Perkin Elmer, Waltham, MA, USA, Aanalyst 400), using the calibration standards for Pt (LabKings, AG Hilversum, The Netherlands) and for W (Perkin Elmer, N9303809).

3.5. Characterization of SiO₂–Al₂O₃ Oxides and Catalysts

3.5.1. X-ray Diffraction (XRD)

XRD diffractograms of SiO₂–Al₂O₃ oxides calcined at 550 °C were obtained with a Rigaku diffractometer (Phillips Xpert) equipped with a Cu anode tube (30 kV, 20 mA), using CuK α radiation. The scan was performed in the range of $2\theta \sim 10\text{--}100^\circ$, with a counting time of $2^\circ/\text{min}$. The different crystalline phases of SiO₂ and Al₂O₃ were identified using the corresponding diffraction data cards JCPDS 10-0425 for Al₂O₃ and JCPDS 29-0085 for SiO₂.

3.5.2. Scanning Electron Microscopy (SEM)

The SiO₂–Al₂O₃ oxides microstructure images were taken by scanning electron microscopy (SEM) with field emission and high resolution in a Joel microscope (model JFM-6701-F, Japan) using secondary electrons.

3.5.3. Optical Microscopy and Textural Analysis of Spray-Dried 25SA Microspheres

The optical microscopy images of the 25SA microspheres spray dried and calcined at 550 °C were obtained through an optical microscope (Biomédica–Lab, Orange City, FL, USA, L1100), using a 10X objective and a 10X ocular. The images were captured with a digital camera (LG–L, Bello) with a resolution of 8 MP, and the particle diameters were measured using a micrometric scale printed on the processed images, which was elaborated from the calibration of the optical microscope, which consisted of superimposing a micrometric ocular (Euromex, Arnhem, Holland) with a 19 mm printed ruler divided into 100 units on a micrometric slide (Euromex, Holland) with a 2 mm printed ruler divided into 200 units.

The N₂ adsorption–desorption isotherms of the 25SA microspheres were determined in a micromeritics equipment (ASAP-2460, USA) utilizing the physisorption of N₂ at -196°C . Before adsorption, the samples received a degassing pretreatment at 300°C for 5 h under vacuum of 1×10^{-4} torr. These results determined the BET specific area, pore volume, and pore diameter distribution by applying the standard BET model [78]. To quantify the pore volume (V_p) of the samples, the T-plot method [79] was used. The pore

diameter distributions were obtained from the BJH model [80], using isotherm desorption and assuming the cylindrical pore geometry.

3.5.4. Temperature Programmed Reduction (TPR)

The TPR profiles of the calcined catalysts were obtained under H₂ flow (10 vol.% H₂/Ar) by a commercial ISRI thermodesorption instrument (multipulse RIG model) equipped with a thermal conductivity detector (TCD). Samples of 500 mg and a gas flow of 25 cm³/min were used in the experiments. The TPR profiles were registered by heating the sample from 25 to 600 °C at a heat rate of 10 °C/min, and a TCD monitored the H₂ consumption rate. The amount of H₂ consumed was obtained by the deconvolution and integration of the TPR peaks using the Peak Fit program. The calibration was done by measuring the change in weight due to a reduction in H₂ of 2 mg of CuO using an electrobalance Cahn-RG. The TPR signal of CuO was made and correlated with the stoichiometric H₂ consumption.

3.5.5. H₂ Chemisorption

Chemisorption measurements of H₂ were performed using a conventional volumetric glass apparatus (base pressure 1 × 10⁻⁶ Torr). The amount of chemisorbed H₂ was determined from adsorption isotherms measured at 25 °C. In a typical experiment, 1 g of catalyst was reduced in H₂ at 550 °C for 1 h, then evacuated at the same temperature for 2 h and cooled down under vacuum to 25 °C. After that, the first adsorption isotherm was measured, and the catalyst was then evacuated to 1 × 10⁻⁵ Torr for 30 min at 25 °C to remove the H₂ physisorbed. The second isotherm of H₂ was carried out until equilibrium. The linear parts of the isotherms were extrapolated to zero pressure. The subtraction of the two isotherms gave the amount of H₂ strongly chemisorbed on metal particles. These values were used to calculate the Pt dispersion (H/Pt ratio or % of active Pt). For the Pt dispersion calculation, the stoichiometry H/Pt was 1, as reported in the literature [81]. In preliminary experiments, it was found that chemisorptions of hydrogen on the 25SA support were negligible at 25 °C. The uncertainty of the reported uptakes was ±0.45 μmol H₂/g_{cat}.

$$\text{Pt dispersion [\%]} = (\text{Pt active atoms} / \text{Total Pt atoms}) \times 100 \quad (3)$$

Pt active atoms were related with the H₂ chemisorption.

3.6. CO Combustion

The conversion during combustion of CO with the catalysts Pt100A, Pt25SA-0.5W, Pt25SA-1W, Pt25SA-4W, Pt25SA-8W, and Pt25SA-16W in the form of microspheres (H₂ reduced at 800 °C) was determined in a fixed-bed continuous reactor packed with 0.5 g catalyst. The reagents and products were analyzed online with a Gow Mac 580 gas chromatograph equipped with a thermal conductivity detector (TCD) heated to 200 °C. A 13X molecular sieve packed column (1/8 in × 8 ft) was used, with an oven and injector port temperature of 50 and 150 °C, respectively, injecting a sample volume of 10 μL. CO, O₂, and CO₂ were analyzed using a flow of 30 cm³/min of He. Before starting the reaction with the mixture containing CO, the catalyst was heated in a stream of H₂/N₂ (10%) of 20 cm³/min from 25 °C to 300 °C (10 °C/min) and was kept at this temperature for 2 h and then cooled to 100 °C to start the reaction.

In the catalytic evaluation, a reaction mixture composed of 7 vol.% CO, 13.5 vol.% O₂ in 79.5 vol.% He was used with a volumetric flow of 200 cm³/min. No internal and external diffusion limitations were observed using this flow and the size of the microspheres. The composition of CO and O₂ was previously verified in each experiment. Under these conditions, the CO/O₂ molar ratio was 1.93, in an attempt to have a slightly oxidizing condition. Mass flow controllers controlled the gas flows (AALBORG, repeatability: ±0.25% of full scale). The reaction temperature changed between 120 and 260 °C, with 20 °C

increments. The reaction time was 25 min at each temperature, including chromatographic analysis. The conversion was calculated on the moles of CO fed according to:

$$X [\%] = [N_{CO}^{\circ} - N_{CO}] / N_{CO}^{\circ} \times 100 \quad (4)$$

where X is the conversion of CO, N_{CO}° are the moles of CO fed, and N_{CO} are the moles of unconverted CO.

4. Conclusions

A catalyst of 0.05% by weight of Pt supported on SiO₂–Al₂O₃ microspheres stabilized with 0.5 wt% W was developed for the combustion of CO which showed a conversion of 50% at 172 °C and a conversion of 90% at 190 °C.

It was found that the addition of small concentrations of W (<1wt% W) to the SiO₂–Al₂O₃ support produces a stabilized surface when the catalyst is subjected to reduction or calcination at a high temperature (800 °C)

It was found that a ratio of 25wt% of SiO₂ and 75wt% of Al₂O₃ can produce spheres with high mechanical resistance to crushing. A straight rectangular vanes atomization disk (DAR) was studied to obtain SiO₂–Al₂O₃–WO_x microspheres of a specific diameter (20–180 μm). DAR produced complete spherical particles. The geometry of the vanes in the disk affected the morphology of the particles obtained. The increase in the speed of rotation of the disks decreased the maximum particle size and the Sauter average diameter in the SiO₂–Al₂O₃ microspheres. Using the DAR with a rotation speed of 6000 rpm is recommended.

From the studies of TPR, Pt dispersion, and BET specific area, a surface model has been suggested where it is proposed that at low W contents (0.5 and 1wt%) and a reduction of 800 °C, it is possible to have Pt particles thermally stabilized by the presence of surface WO_x.

Author Contributions: Conceptualization, J.L.C. and A.P.-G.; methodology, J.L.C., A.P.-G. and J.P.-C.; investigation, A.P.-G. and J.P.-C.; resources, J.L.C., B.Z., T.V., J.S. and M.A.G.-L.; data curation, J.L.C.; writing—preparing the initial draft, A.P.-G.; critical writing—review and editing, J.L.C., J.S., A.P.-G., B.Z. and T.V.; visualization, A.P.-G.; supervision, J.L.C.; project administration, J.L.C.; procurement of funds, J.L.C. All authors have read and agreed to the published version of the manuscript.

Funding: This research received no external funding.

Acknowledgments: This work was carried out in collaboration with the Azcapotzalco Autonomous Metropolitan University, the National Polytechnic Institute (ESIQIE), and the Mexican Petroleum Institute (IMP). Arturo Pallares expresses his gratitude to the UAM for the postgraduate scholarship granted to carry out doctoral studies. Arturo P. is also grateful for the loan of the spray-drying equipment from the UAM-A and the Catalysis and Processes Laboratories of the Chemical Industry belonging to the UAM-A. José L. Contreras appreciates the support received from the company Síntesis y Aplicaciones Industriales S.A.

Conflicts of Interest: The authors declare no conflict of interest.

Appendix A. 25SA Suspension Rheology

The rheological behavior of the suspension that was fed to the atomizer of the spray dryer was of particular importance since it characterizes the flowability of the suspension and can also be related to the transport capacity of the fluid due to the pump. It can also provide insight into the repeatability of microsphere formation and is helpful for atomizer design purposes.

The Herschel–Bulkley regression model (Equation (A1)) was fitted to the experimental values in the flow curve of the 25SA suspension (Figure A1a) [82,83]. The model relates the parameters of the shear stress (τ) with the strain rate ($\dot{\gamma}$) by the equation:

$$\tau = \tau_0 + k\dot{\gamma}^n \quad (A1)$$

where τ_0 is the yield shear stress, k is the consistency factor, and n is the flow behavior index. The values of the model parameters estimated by the rheometer software were $\tau_0 = 0.6$ Pa, $k = 24.8$ Pa \cdot n y $n = 0.263$. For $n < 1$, the Herschel–Bulkley fluid is considered shear-thinning.

The viscosity curve of the 25SA suspension (Figure A1b) follows a non-linear behavior, highly thinning with the increase of the shear rate and characteristic of a non-Newtonian pseudoplastic fluid. The decrease in the viscosity of the suspension is associated with the existence of an intraparticula network at rest, which undergoes a gradual rupture with the increase of the applied shear rate [84,85], which makes the particles randomly oriented at rest align with the used shear.

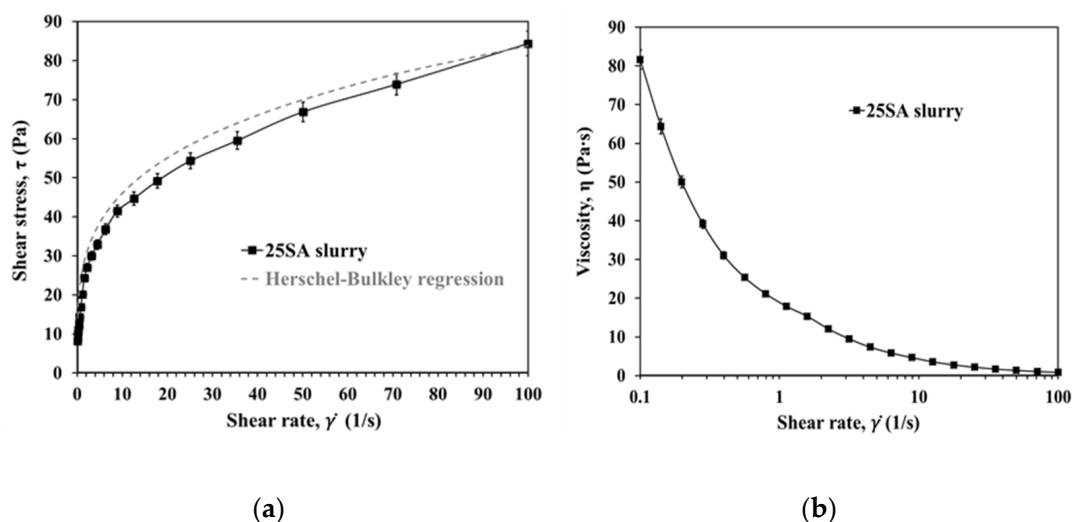


Figure A1. (a) Flow curve; (b) viscosity curve of the 25SA suspension. The relative error percentages for the shear stress and viscosity values were $\pm 1.9\%$ and $\pm 1.5\%$, respectively.

Appendix B

Appendix B.1. Description of the Spray Dryer and Its Operating Parameters

The experiments were carried out in a parallel flow pilot scale spray dryer (Figure A2), using a pneumatically driven rotary disk atomizer. The 25SA suspension at 20 °C was fed utilizing a peristaltic pump (ProMinet, beta/4), with a flow rate of 0.4 cm³/s to the atomizer.

As a heat source for the dryer, a hot combustion gas from a direct combustion LPG gas burner (Riello 40 GS) was used. The combustion gas entered the drying chamber through a volute-type gas disperser located on the lid of the drying chamber with a volumetric flow of 0.14 m³/s. In all experiments, the inlet and outlet drying gas temperatures were 225 \pm 10 °C and 160 \pm 4 °C, respectively.

The dryer used an extractor to aspirate the generated microspheres and spent gas from the drying chamber, and then transport them to the dust separators. The microspheres were collected in a cyclone-type particle separator and in a filter bag.

Appendix B.2. Experiments to Obtain Microspheres with Two Disk Atomizers

Two atomization disks with vanes of different geometry were manufactured from 316 stainless steel. The designs consisted of a straight radial rectangular vanes (DAR) disk (Figure A3a) and a curved rectangular vanes (DAC) disk (Figure A3b). The structure of the discs incorporates a hollow circular chamber (1), a central part in the form of an inverted plate (2), and a threaded connection (3) that holds the disc to the impeller of the atomizer. At the periphery of the disks, 16 liquid ejection channels were located (4). The upper plate (5) covers the vanes and a large part of the disk.

The geometric dimensions of the liquid ejection channels of the DAR and DAC are shown in Figure A3c,d, respectively. The cross-sectional area and volume of the RAD

channel were $17.2 \pm 0.85 \text{ mm}^2$ and $163 \pm 9.8 \text{ mm}^3$, respectively. On the other hand, the cross-sectional area and the volume of the DAC channel were $18.2 \pm 0.89 \text{ mm}^2$ and $164.2 \pm 9.8 \text{ mm}^3$, respectively. The diameter and thickness of the disks were 50 ± 0.1 and $10 \pm 0.1 \text{ mm}$ (Figure A3e,f), respectively.

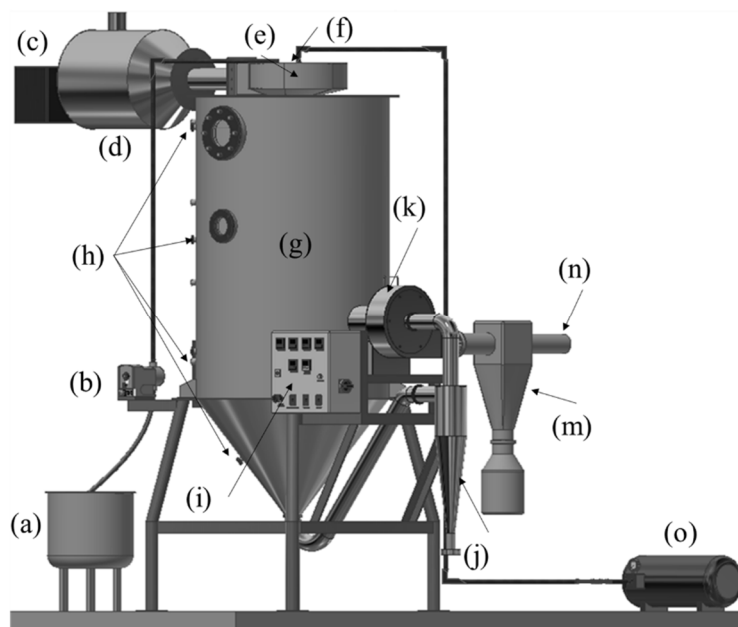


Figure A2. Schematic representation of the spray dryer used to produce the $\text{SiO}_2\text{-Al}_2\text{O}_3$ microspheres. (a) Feed tank, (b) peristaltic pump, (c) direct combustion burner, (d) combustion chamber, (e) gas disperser, (f) rotary atomizer, (g) drying chamber, (h) thermocouples, (i) control panel, (j) cyclone dust separator, (k) extractor, (m) bag filter, (n) spent gas outlet, and (o) air compressor.

Four experiments were performed for each atomization disc design, varying the rotational speed of the discs in the range of 3000 to 14,000 rpm (Table A1).

The rotational speeds of the discs were measured using a digital laser rpm counter tachometer (Tach Tester, TD-2234C+) before the experiments and feeding the suspension into the discs. All rotational speeds of the disk were measured in triplicate.

Measurement of physical properties and characterization analyzes were carried out on microspheres collected from the cyclone separator, which were then calcined in an oven (Thermo Scientific, FB1415M) at $550 \text{ }^\circ\text{C}$ for 6 h with a heating rate of $3 \text{ }^\circ\text{C}/\text{min}$. Also, four selected products were calcined at $750 \text{ }^\circ\text{C}$ for 6 h to perform textural properties analysis. The purpose of calcination was to eliminate organic materials and obtain a porous and rigid structure of the particles.

The apparent density of the products calcined at $550 \text{ }^\circ\text{C}$ was determined by the ratio of the weight of a sample measured on an analytical balance (Sartorius, Göttingen, Germany, BL210S) and its volume occupied in a 10 cm^3 glass graduated cylinder (Pyrex, Mexico). All densities were measured in duplicate.

The elaboration of the particle-size distribution (PSD) and the calculation of the Sauter mean diameter (SMD) was carried out with the use of the Image J processing program of the optical microscopy images, following the methodology described in Masters [20]. The PSD curves were made from the frequency of particle appearance $f_N(D)$ against a representative particle diameter (D). The subscript N indicates the number of particles counted. SMD had the same surface-to-volume ratio of powder sample and was calculated as [20,86]:

$$\text{SMD} = \frac{\sum N_i D_i^3}{\sum N_i D_i^2} \quad (\text{A2})$$

where i denotes the size range considered, N_i is the number of particles in size range i , and D_i is the middle diameter of size range i .

Table A1. Atomization parameters established in the experiments with a flow rate of $0.4 \text{ cm}^3/\text{s}$.

	Straight Rectangular Vanes Disc				Curved Rectangular Vanes Disc			
Disc rotation speed ¹ , (rpm)	P1-DAR 3000	P2-DAR 6000	P3-DAR 11,500	P4-DAR 14,000	P1-DAC 3000	P2-DAC 6000	P3-DAC 11,500	P4-DAC 14,000

The absolute error of the rotational speed of disk ¹ was ± 85 rpm.

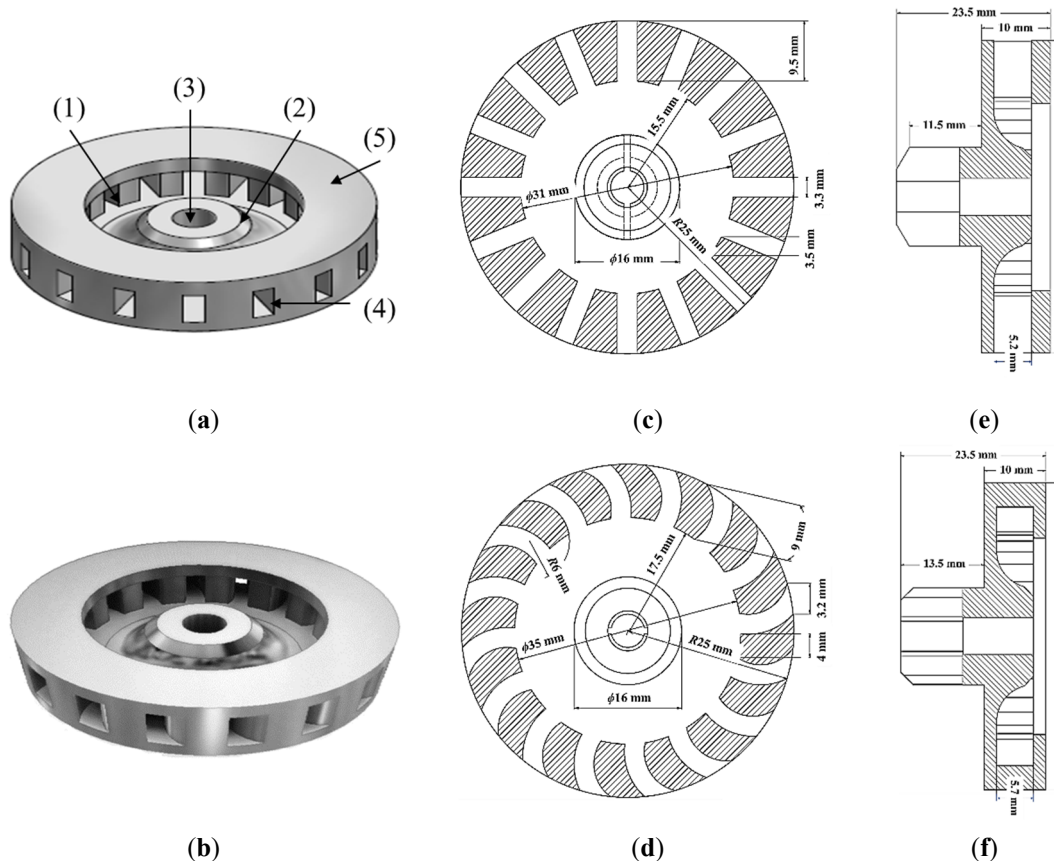


Figure A3. Shape and dimensions (absolute error of ± 0.1 mm) of the atomization discs (a,b) form and structure; (c,d) interior view; (e,f) side view of the straight rectangular vanes disk and the curved rectangular vanes disk, respectively.

Appendix B.3. Spray-Dried 25SA Microspheres Obtained with the Curved Rectangular Vanes Disk

With the curved rectangular vanes disk (DAC), microspheres of various sizes and fragmented hollow particles (eggshell type) were produced (Figure A4a–d). In the products of the experiments P1-DAC (Figure A4a), P2-DAC (Figure A4b), and P3-DAC (Figure A4c), the presence of laminar particles with irregular edges can also be observed, which were due to the deposition of material on the walls of the drying chamber. These particles were then detached and exited together with the other particles of the dryer. It is notable that the geometry of the curved vanes on the atomization disk led to the increased production of fragmented particles.

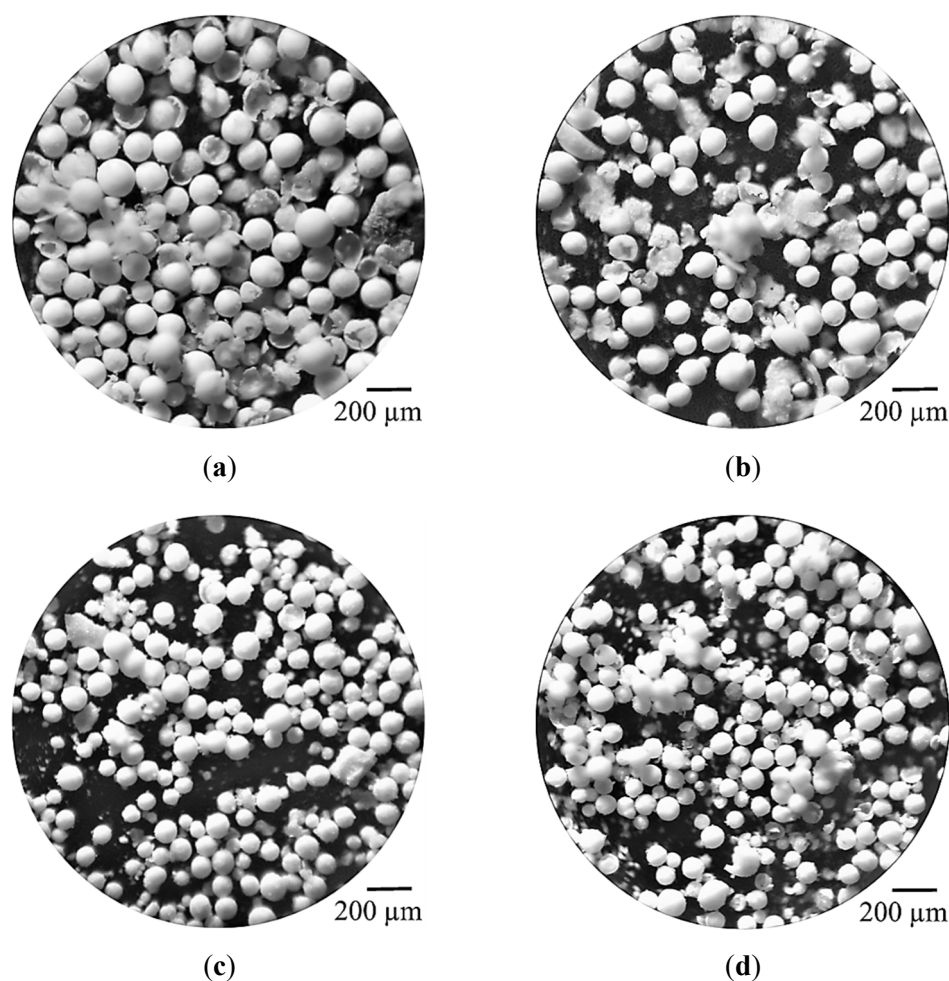


Figure A4. Optical microscopy of the spray-dried 25SA microspheres and calcined at 550 °C was obtained with the curved rectangular vanes disk: (a) P1-DAC; (b) P2-DAC; (c) P3-DAC; (d) P4-DAC.

Appendix B.4. Effect of the DAC-Disk Rotation Speeds on the Particle-Size Distributions (PSD) and the Sauter Mean Diameter (SMD)

Similarly to what happened with the DAR atomizer, when the rotational disk speed was decreased in the experiment P1-DAC (3000 rpm) (Figure A5a), the PSD extended to the right to a greater range of diameter of particle size of 10–230 μm , with a maximum value in the particle diameter of 70 μm .

On the other hand, the PSDs of the P2-DAC (6000 rpm) (Figure A5b) and P3-DAC (11,500 rpm) (Figure A5c) products were very similar and slightly skewed to the right, with a maximum value at a particle diameter of 50 μm , with particle diameter ranges of 10–210 and 10–170 μm , respectively (Table 2). When the speed of rotational disk was increased, the PSD of the P4-DAC product (14,000 rpm) (Figure A5d) was equally skewed to the right, presenting its maximum value at the particle diameter of 30 μm , whose particle diameter range was 10–150 μm .

The previous results again indicated that the maximum particle diameter increased when the rotation speed of the curved blades disk decreased.

It is important to note that larger maximum particle diameters were achieved with the DAC, which is attributed to a more significant amount of air occluded inside the disk and consequently in the atomized suspension when the disk rotates at high speed, which makes the particles inflate or break during the drying period [25,87–90]. However, the minimum particle diameter was 10 μm for all 25SA products or powders.

On the other hand, the Sauter mean diameter (SMD) of the microspheres obtained with the DAC atomizer was slightly more significant than the microspheres obtained with the DAR atomizer (Table 1). The SMD of the P1–DAC, P2–DAC, P3–DAC, and P4–DAC products were 117, 101, 81, and 73 μm , respectively, again observing that with the increase in the disk rotation speed, the SMD of the particle of the products decreased.

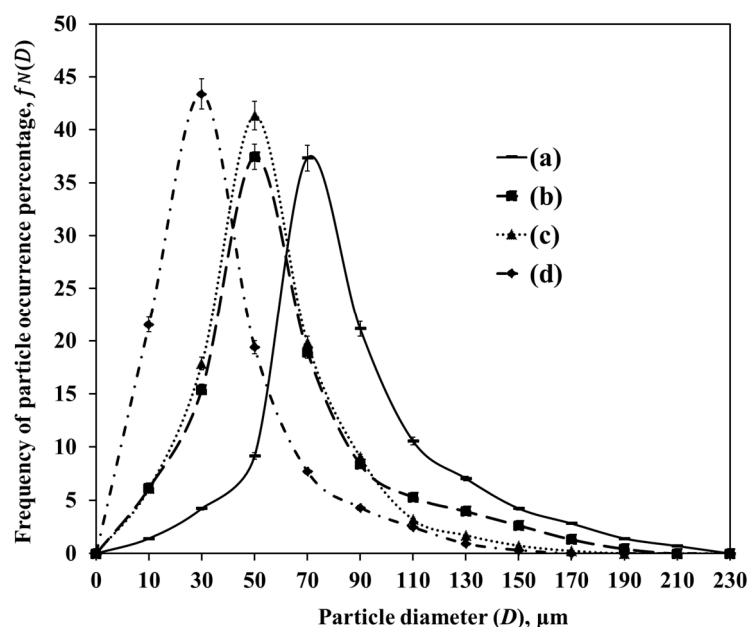


Figure A5. Particle diameter distributions of spray-dried 25SA products calcined at 550 °C, obtained at the following rotational speeds of the curved rectangular vanes disk: (a) 3000 rpm (P1–DAC), (b) 6000 rpm (P2–DAC), (c) 11,500 rpm (P3–DAC), and (d) 14,000 rpm (P4–DAC).

References

- Sadeghbeigi, R. *Fluid Catalytic Cracking Handbook*, 3rd ed.; Butterworth–Heinemann: Waltham, MA, USA, 2012; pp. 117–123.
- Moreno-Montiel, N. Modelamiento de un Reactor de Microactividad para la Evaluación de Catalizadores del Proceso de Desintegración Catalítica: Modelos de Desintegración y Desactivación. Ph.D. Thesis, Metropolitan Autonomous University—Iztapalapa, Mexico City, Mexico, 2004.
- Vaarkamp, M.; Matheson-Stockwell, D. CO Oxidation Promoters for Use in FCC Processes. U.S. Patent 7,959,792, 14 June 2011.
- Melloa, F.L.; Gobbo, R.; Moure, G.T.; Miracca, I. Oxy–Combustion Technology Development for Fluid Catalytic Crackers (FCC)—Large Pilot Scale Demonstration. *Energy Procedia* **2013**, *37*, 7815–7824. [[CrossRef](#)]
- Chiranjeevi, T.; Ravichander, N.; Gokak, D.T.; Ravikumar, V.; Choudary, N.V. The Selection of Fluid Catalytic Cracking Catalysts and Additives: The Significance of Attrition Studies. *Petrol. Sci. Technol.* **2014**, *32*, 470–478. [[CrossRef](#)]
- de Carvalho, M.C.N.A.; Morgado, E., Jr.; Cerqueira, H.S.; Resende, N.S.; Schmal, M. Behavior of Fresh and Deactivated Combustion Promoter Additives. *Ind. Eng. Chem. Res.* **2004**, *43*, 3133–3136. [[CrossRef](#)]
- Blanton, W.A., Jr. NOx Control in Platinum–Promoted Complete Combustion Cracking Catalyst Regeneration. U.S. Patent 4,290,878, 22 September 1981.
- Cheng, W.C.; Kim, G.; Peters, A.W.; Zhao, X.; Rajagopalan, K.; Ziebarth, M.S.; Pereira, C.J. Environmental Fluid Catalytic Cracking Technology. *Catal. Rev. Sci. Eng.* **1998**, *40*, 39–79. [[CrossRef](#)]
- Venuto, P.B.; Habib, E.T., Jr. *Fluid Catalytic Cracking with Zeolite Catalysts*; Marcel Dekker, Inc.: New York, NY, USA, 1979; pp. 47–132.
- Kennedy, J.V.; Dight, L.B. Catalytic Cracking. U.S. Patent 4,214,978, 29 July 1980.
- Fraenkel, D.; Moselle, I.L. CO Oxidation Promoter and Use thereof for Catalytic Cracking. U.S. Patent 5,565,399, 15 October 1996.
- Child, J.E. NOx Control in Fluidized Bed Combustion. U.S. Patent 4,812,431, 14 March 1989.
- Avidan, A.A. Circulating Fluid Bed Combustion with CO Combustion Promoter and Reduced Combustion Air. U.S. Patent 4,927,348, 22 May 1990.
- Chester, W.A. CO Combustion Promoters: Past and Present. In *Fluid Catalytic Cracking VII: Materials, Methods and Process Innovations*, 1st ed.; Ocelli, M.L., Ed.; Elsevier Science & Technology: Oxford, UK, 2007; Volume 166, pp. 67–77.
- Silverman, L.D.; Speronello, B.K. Catalytic Cracking with Mullite Composition Promoted Combustion of Carbon Monoxide. U.S. Patent 4,608,357, 26 August 1986.

16. Guisnet, M.; Mignard, S. Fluid Catalytic Cracking: Process, Catalyst and Chemistry. *Actual. Chim.* **2000**, *2*, 14–22.
17. Passos, M.L.; Birchall, V.S. Manipulating Physical Properties of Powder. In *Spray Drying Technology*, 1st ed.; Woo, M.W., Mujumdar, A.S., Daud, W.R.W., Eds.; Publisher: Singapore, 2010; Volume 1, pp. 37–60.
18. Lukasiewicz, S.J. Spray–Drying Ceramic Powders. *J. Am. Ceram. Soc.* **1989**, *72*, 617–624. [[CrossRef](#)]
19. Fletcher, D.F.; Guo, B.; Harvie, D.J.E.; Langrish, T.A.G.; Nijdam, J.J.; Williams, J. What is Important in the Simulation of Spray Dryer Performance and How do Current CFD Models Perform? *Appl. Math. Model.* **2006**, *30*, 1281–1292. [[CrossRef](#)]
20. Masters, K. *Spray Drying Handbook*, 5th ed.; Longman Scientific & Technical: London, UK, 1991.
21. Anandharamkrishnan, C.; Ishwarya, S.P. *Spray Drying Techniques for Food Ingredient Encapsulation*, 1st ed.; John Wiley & Sons: Chicago, IL, USA, 2015; pp. 1–36.
22. Filková, I.; Huang, L.X.; Mujumdar, A.S. Industrial Spray Drying Systems. In *Handbook of Industrial Drying*, 4th ed.; Mujumdar, A.S., Ed.; CRC Press: Boca Raton, FL, USA, 2014; Volume 10, pp. 216–256.
23. Moyers, C.G.; Baldwin, G.W. Psychrometry, Evaporative Cooling, and Solids Drying. In *Perry's Chemical Engineers' Handbook*, 7th ed.; Perry, R.H., Green, D.W., Eds.; McGraw-Hill: New York, NY, USA, 1997; Volume 7, pp. 12-1–12-90.
24. Nielse, K. Atomizer Wheel for the Atomization of Suspensions of Hard–Wearing Materials. U.S. Patent 3,454,226, 8 July 1969.
25. Hansen, O.E. Atomizer Wheel for the Atomization of Liquids. U.S. Patent 4,303,200, 1 December 1981.
26. Jensen, A.N.; Pisecky, J. Atomizer Wheel for Use in a Spray Drying Apparatus. U.S. Patent 4,733,821, 29 March 1988.
27. Svarrer, L. Atomizer Wheel with Steel Bushings. U.S. Patent 4,684,065, 4 August 1987.
28. Svendsen, G. Rotary Atomizer and a Method of Operating It. U.S. Patent 5,518,180, 21 May 1996.
29. Contreras, J.L.; Fuentes, G.A.; Salmones, J.; Zeifert, B. Thermal Stability of Pt Nanoparticles Supported on WO_x/Al₂O₃ for n-Heptane Hydroconversion. *Mat. Res. Soc. Proc.* **2010**, *1279*, 123–141. [[CrossRef](#)]
30. Contreras, J.L.; Fuentes, G.A.; García, L.A.; Salmones, J.; Zeifert, B. WO_x Effect on the Catalytic Properties of Pt Particles on Al₂O₃. *J. Alloys Compd.* **2009**, *483*, 450–452. [[CrossRef](#)]
31. Hernández, I.P.; Gochi-Ponce, Y.; Contreras, J.L.; Fernández, A.M. Steam Reforming of Ethanol over Nickel-Tungsten Catalyst. *Int. J. Hydrog. Energy* **2010**, *35*, 12098–12104. [[CrossRef](#)]
32. Zhao, R.; Goodwin Jr., J.G.; Oukaci, R. Attrition Assessment for Slurry Bubble Column Reactor Catalysts. *Appl. Catal. A Gen.* **1999**, *189*, 99–116. [[CrossRef](#)]
33. Trunov, M.A.; Schoenit, M.; Zhu, X.; Dreizin, E.L. Effect of Polymorphic Phase Transformations in Al₂O₃ Film on Oxidation Kinetics of Aluminum Powders. *Combust. Flame* **2005**, *140*, 310–318. [[CrossRef](#)]
34. Ozawa, M.; Hashimoto, K.; Suzuki, S. High–Temperature Structural Change of Catalytic MnO_x-LaO_x-Al₂O₃ Powder for Lean-Exhaust NO_x Removal Treatment. *J. Mater. Sci.* **2001**, *36*, 1401–1405. [[CrossRef](#)]
35. Wickrsheim, K.A.; Korpi, G.K. Interpretation of the Infrared Spectrum of Boehmite. *J. Chem. Phys.* **1965**, *42*, 579–583. [[CrossRef](#)]
36. Sun, J.; Xu, Z.; Li, W.; Shen, X. Effect of Nano-SiO₂ on the Early Hydration of Alite-Sulphoaluminate Cement. *Nanomaterials* **2017**, *7*, 102. [[CrossRef](#)]
37. Diaz, C.; Valenzuela, M.L.; Cifuentes-Vaca, O.; Segovia, M.; Laguna-Bercero, M.A. Incorporation of NiO into SiO₂, TiO₂, Al₂O₃, and Na_{4.2}Ca_{2.8}(Si₆O₁₈) Matrices: Medium Effect on the Optical Properties and Catalytic Degradation of Methylene Blue. *Nanomaterials* **2020**, *10*, 2470. [[CrossRef](#)]
38. Ivanova, A.S.; Slavinskaya, E.M.; Gulyaev, R.V.; Zaikovskii, V.I.; Stonkus, O.A.; Danilova, I.G.; Plyasova, L.M.; Polukhina, I.A.; Boronin, A.I. Metal–Support Interactions in Pt/Al₂O₃ and Pd/Al₂O₃ Catalysts for CO Oxidation. *Appl. Catal. B Environ.* **2010**, *97*, 57–71. [[CrossRef](#)]
39. Huang, L.X.; Mujumdar, A.S. The Effect of Rotary Disk Atomizer RPM on Particle Size Distribution in a Semi–Industrial Spray Dryer. *Dry. Technol.* **2008**, *26*, 1319–1325. [[CrossRef](#)]
40. Filková, I.; Weberschinke, J. Effect of Vane Geometry on Droplet Size and Size Distribution in Spray Dryer. In *Drying'80*; Mujumdar, A.S., Ed.; Hemisphere/McGraw–Hill: New York, NY, USA, 1980; Volume 2, pp. 417–424.
41. Ahmed, M.; Youssef, M.S. Characteristics of Mean Droplet Size Produced by Spinning Disk Atomizers. *J. Fluids Eng.* **2012**, *134*, 1–9. [[CrossRef](#)]
42. Ahmed, M.; Youssef, M.S. Influence of Spinning Cup and Disk Atomizer Configurations on Droplet Size and Velocity Characteristics. *Chem. Eng. Sci.* **2014**, *107*, 149–157. [[CrossRef](#)]
43. Peng, H.; Shan, X.; Ling, X.; Wang, D.; Li, J. Ligament–Type Granulation of Molten Slag in Different Rotary Disk Configurations. *Appl. Therm. Eng.* **2018**, *128*, 1565–1578. [[CrossRef](#)]
44. Sonwane, C.G.; Ludovice, P.J. A Note on Micro–and Mesopores in the Walls of SBA–15 and Hysteresis of Adsorption Isotherms. *J. Mol. Catal. A Chem.* **2005**, *238*, 135–137. [[CrossRef](#)]
45. Ryoo, R.; Jun, S.; Kim, J.M.; Kim, M.J. Generalised Route to the Preparation of Mesoporous Metallosilicates via Post–Synthetic Metal Implantation. *Chem. Commun.* **1997**, *41*, 2225–2226. [[CrossRef](#)]
46. Esparza, J.M.; Ojeda, M.L.; Campero, A.; Hernández, G.; Felipe, C.; Asomoza, M.; Cordero, S.; Kornhauser, I.; Rojas, F. Development and Sorption Characterization of some Model Mesoporous and Microporous Silica Adsorbents. *J. Mol. Catal. A Chem.* **2005**, *228*, 97–110. [[CrossRef](#)]
47. Brunauer, S. *The Adsorption of Gases and Vapours*; Oxford University Press: London, UK, 1944.

48. Thomas, R.; van Oers, E.M.; de Beer, V.H.J.; Moulijn, J.A. Characterization of silica-supported molybdenum oxide and tungsten oxide. Reducibility of the oxidic state versus hydrodesulfurization activity of the sulfided state. *J. Catal.* **1983**, *84*, 275–287. [[CrossRef](#)]
49. Regalbuto, J.R.; Wolf, E.E. An Integrated Study of Pt/WO₃/SiO₂ Catalysts for the NO-CO Reaction: I. Catalyst Characterization by XRD, Chemisorption, and XPS. *J. Catal.* **1987**, *107*, 114–128. [[CrossRef](#)]
50. Scelza, O.A.; De Miguel, S.R.; Baronetti, G.T.; Castro, A.A. Performance of Pt–Re/Al₂O₃ Catalysts with Different Radial Distribution Profiles. *React. Kinet. Catal. Lett.* **1987**, *33*, 143–148. [[CrossRef](#)]
51. Yao, H.C.; Sieg, M.; Plummer, H.K., Jr. Surface interactions in the Pt/γ-Al₂O₃ system. *J. Catal.* **1979**, *59*, 365–374. [[CrossRef](#)]
52. McNicol, B.D.; Short, R.T. The Reducibility of Ru, Pt/Ru and Pt Oxide Electrocatalysts as Measured by Temperature-Programmed Reduction and Cyclic Voltammetry. *J. Electroanal. Chem. Interf. Electrochem.* **1978**, *92*, 115–120. [[CrossRef](#)]
53. Lieske, H.; Lietz, G.; Spindler, H.; Völter, J. Reactions of Platinum in Oxygen- and Hydrogen-Treated Pt/γ-Al₂O₃ Catalysts: I. Temperature-Programmed Reduction, Adsorption, and Redispersion of Platinum. *J. Catal.* **1983**, *81*, 8–16. [[CrossRef](#)]
54. Dautzenberg, F.M.; Wolters, H.B.M. State of Dispersion of Platinum in Alumina-Supported Catalysts. *J. Catal.* **1978**, *51*, 26–39. [[CrossRef](#)]
55. Hurst, N.W.; Gentry, S.J.; Jones, A.; McNicol, B.D. Temperature Programmed Reduction. *Catal. Rev.* **1982**, *24*, 233–309. [[CrossRef](#)]
56. M'Boungou, J.S.; Schmitt, J.L.; Maire, G.; Garin, F. Role of Tungsten in Supported Pt-W Reforming Catalysts Part I. Modification of Platinum Activity and Selectivity by Addition of Tungsten. *Catal. Lett.* **1991**, *10*, 391–400. [[CrossRef](#)]
57. Ruckenstein, E.; Pulvermacher, B. Effect of the Pore Size on the Aging of Supported Metals. *J. Catal.* **1975**, *37*, 416–423. [[CrossRef](#)]
58. M'Boungou, J.S.; Hilaire, L.; Maire, G.; Garin, F. Role of Tungsten in Supported Pt-W Reforming Catalysts Part II. Influence of the tungsten loading and metal-support interactions effect. *Catal. Lett.* **1991**, *10*, 401–411. [[CrossRef](#)]
59. Park, J.W.; Thomas, K.; Gestel, J.V.; Gilson, J.P.; Collet, C.; Dath, J.P.; Houalla, M. Study of Ir/WO₃/Al₂O₃ Ring Opening Catalysts. *Appl. Catal. A Gen.* **2010**, *388*, 37–44. [[CrossRef](#)]
60. Contreras, J.L.; Fuentes, G.A.; Zeifert, B.; Salmones, J. Stabilization of Supported Platinum Nanoparticles on γ-Alumina Catalysts by Addition of Tungsten. *J. Alloys Compd.* **2009**, *483*, 371–373. [[CrossRef](#)]
61. Alexeev, O.; Gates, B. EXAFS characterization of supported metal-complex and metal-cluster catalysts made from organometallic precursors. *Top. Catal.* **2000**, *10*, 273–293. [[CrossRef](#)]
62. Contreras, J.L.; Figueroa, A.; Zeifert, B.; Salmones, J.; Fuentes, G.A.; Vazquez, T.; Angeles, D.; Nuño, L. Production of Hydrogen by Ethanol Steam Reforming using Ni-Co-ex-Hydrotalcite Catalysts, Stabilized with Tungsten Oxides. *Int. J. Hydrog. Energy* **2021**, *46*, 6474–6493. [[CrossRef](#)]
63. Regalbuto, J.R.; Allen, C.W.; Wolf, E.E. An Integrated Study of Pt/WO₃/SiO₂ Catalysts for the NO-CO Reaction. II. TEM Investigation of Overlayer Formation on Model Pt-WO₃/SiO₂ Catalysts. *J. Catal.* **1987**, *108*, 304–322. [[CrossRef](#)]
64. Yermakov, Y.I. Anchored Complexes in Fundamental Catalytic Research. *Stud. Surf. Sci. Catal.* **1981**, *7*, 57–76.
65. Regalbuto, J.R.; Wolf, E.E. An Integrated Study of Pt/WO₃/SiO₂ Catalysts for the NO-CO Reaction III. FTIR Kinetic Study and Correlation of Promotional Effects. *J. Catal.* **1988**, *109*, 12–24. [[CrossRef](#)]
66. Grisel, R.J.H.; Slyconish, J.J.; Niewenhuys, B.E. Oxidation Reactions over Multi-Component Catalysts: Low-Temperature CO Oxidation and the Total Oxidation of CH₄. *Top. Catal.* **2001**, *16*, 425–431. [[CrossRef](#)]
67. Bourane, A.; Bianchi, D. Oxidation of CO on a Pt/Al₂O₃ Catalyst: From the Surface Elementary Steps to Lighting-Off Tests: II. Kinetic Study of the Oxidation of Adsorbed CO Species Using Mass Spectroscopy. *J. Catal.* **2002**, *209*, 114–125. [[CrossRef](#)]
68. Gu, L.; Chen, X.; Zhou, Y.; Zhu, Q.; Huang, H.; Lu, H. Propene and CO Oxidation on Pt/Ce-Zr-SO₄²⁻ Diesel Oxidation Catalysts: Effect of Sulfate on Activity and Stability. *Chin. J. Catal.* **2017**, *38*, 607–615. [[CrossRef](#)]
69. Thormählen, P.; Skoglundh, M.; Fridell, E.; Anderson, B. Low-Temperature CO Oxidation over Platinum and Cobalt Oxide Catalysts. *J. Catal.* **1999**, *188*, 300–310. [[CrossRef](#)]
70. Padilla, R.; Benito, M.; Rodríguez, L.; Serrano-Lotina, A.; Daza, L. Platinum Supported Catalysts for Carbon Monoxide Preferential Oxidation: Study of Support Influence. *J. Power Sources* **2009**, *192*, 114–119. [[CrossRef](#)]
71. Manasilp, A.; Gulari, E. Selective CO Oxidation over Pt/Alumina Catalysts for Fuel Cell Applications. *Appl. Catal. B Environ.* **2002**, *37*, 17–25. [[CrossRef](#)]
72. Akil, J.; Siffert, S.; Laurence, P.R.; Debecker, D.P.; Devred, F.; Cousin, R.; Poupin, C. Effect of Precious Metals on NO Reduction by CO in Oxidative Conditions. *Appl. Sci.* **2020**, *10*, 3042. [[CrossRef](#)]
73. Wilson, R.C. Method of Regenerating a Hydrocarbon Conversion Catalyst to Minimize Carbon Monoxide in Regenerator Effluent. U.S. Patent 3,808,121, 30 April 1974.
74. Gupta, R.P. Fluidizable Particulate Materials and Methods of Making Same. U.S. Patent 5,972,835, 26 October 1999.
75. Nayak, B.B.; Mishra, P.K.; Tripathy, H.K.; Acharya, B.S. Jet-Wheel Impact Atomizer for Spray Drying and a Process for the Preparation of Finely Dispersed Spray of Slurry/Liquid. Patent WO 2007/096905, 30 August 2007.
76. Nayak, B.B.; Mishra, P.K.; Tripathy, H.K.; Acharya, B.S. Jet-Wheel Impact Atomizer for Spray Drying. U.S. Patent 7,829,041, 9 November 2010.
77. Karakonstantis, K.; Bourikas, K.; Lycourghiotis, A. Tungsten-Oxo-Species Deposited on Alumina. I. Investigation of the Nature of the Tungstates Deposited on the Interface of the γ-Alumina/Electrolyte Solutions at Various pH's. *J. Catal.* **1996**, *162*, 295–305. [[CrossRef](#)]

78. Brunauer, S.; Emmett, P.H.; Teller, E. Adsorption of Gases in Multimolecular Layers. *J. Am. Chem. Soc.* **1938**, *60*, 309–319. [[CrossRef](#)]
79. Lippens, B.C.; Boer, J.H. Studies on Pore Systems in Catalysts: V. The t Method. *J. Catal.* **1965**, *4*, 319–323. [[CrossRef](#)]
80. Barrett, E.P.; Joyner, L.G.; Halenda, P.P. The Determination of Pore Volume and Area Distributions in Porous Substances. I. Computations from Nitrogen Isotherms. *J. Am. Chem. Soc.* **1951**, *73*, 373–380. [[CrossRef](#)]
81. Prasad, J.; Murthy, K.R.; Menon, P.G. The Stoichiometry of Hydrogen-Oxygen Titrations on Supported Platinum Catalysts. *J. Catal.* **1978**, *52*, 515–520. [[CrossRef](#)]
82. Holdsworth, S.D. Rheological Models used for the Prediction of the Flow Properties of Food Products: A Literature Review. *Trans. Inst. Chem. Eng. Part C.* **1993**, *71*, 139–179.
83. Rao, M.A. Flow and Functional Models for Rheological Properties of Fluid Foods. In *Rheology of Fluid, Semisolid, and Solid Foods*, 2nd ed.; Rao, M.A., Ed.; Food Engineering Series: Boston, MA, USA, 2014; pp. 27–58.
84. Mishra, P.K.; Nayak, B.B.; Mishra, B.K. Influence of Behaviour of Alumina Slurry on Quality of Alumina Powder Prepared by Jet Wheel Impact Atomization. *Powder Technol.* **2009**, *196*, 272–277. [[CrossRef](#)]
85. Pradhan, M.; Bhargava, P. Influence of Sucrose Addition on Rheology of Alumina Slurries Dispersed with a Polyacrylate Dispersant. *J. Am. Ceram. Soc.* **2005**, *88*, 833–838. [[CrossRef](#)]
86. Lefebvre, A.H.; McDonell, V.G. *Atomization and Sprays*, 2nd ed.; CRC Press: Boca Raton, FL, USA, 2017; pp. 55–70.
87. Handscomb, C.S.; Kraft, M.; Bayly, A.E. A New Model for the Drying of Droplets Containing Suspended Solids. *Chem. Eng. Sci.* **2009**, *64*, 228–246. [[CrossRef](#)]
88. Elversson, J.; Millqvist-Fureby, A.; Alderborn, G.; Elofsson, U. Droplet and Particle Size Relationship and Shell Thickness of Inhalable Lactose Particles during Spray Drying. *J. Pharm. Sci.* **2003**, *92*, 900–910. [[CrossRef](#)]
89. Walton, D.E. The Morphology of Spray-dried Particles a Qualitative View. *Dry. Technol.* **2000**, *18*, 1943–1986. [[CrossRef](#)]
90. Alamilla-Beltrán, L.; Chanona-Pérez, J.J.; Jiménez-Aparicio, A.R.; Gutiérrez-López, G.F. Description of Morphological Changes of Particles along Spray Drying. *J. Food Eng.* **2005**, *67*, 179–184. [[CrossRef](#)]